

DESIGN, FABRICATION, AND IMPLEMENTATION OF THE ENERGETIC  
PARTICLE INTEGRATING SPACE ENVIRONMENT MONITOR  
INSTRUMENT

by

Adam Kristopher Gunderson

A thesis submitted in partial fulfillment  
of the requirements for the degree

of

Master of Science

in

Electrical Engineering

MONTANA STATE UNIVERSITY  
Bozeman, Montana

July, 2014

© COPYRIGHT

by

Adam Kristopher Gunderson

2014

All Rights Reserved

## ACKNOWLEDGEMENTS

I would like to thank Dr. David Klumpar and Larry Springer for bringing me onto this thesis, for their technical advice and helping me complete this project as well as Dr. Brock LaMeres and Dr. Todd Kaiser for advising me. I would also like to thank two Matthew Handley, Jerry Johnson, Andrew Crawford, Keith Mashburn, Ehson Mosleh, and the rest of the Space Science and Engineering. Who helped immensely in the mechanical and software design as well as supporting the large amount of testing that this project required.

## VITA

Adam Kristopher Gunderson served as an Electronics Technician in the US Navy for six years where he focused on the repair and maintenance of communication and navigational equipment. He graduated with a B.S. in Electrical Engineering from Montana State University in 2012. Adam has worked for the Space Science and Engineering Lab since 2008 on the Explorer 1 Prime, FIREBIRD-I and FIREBIRD-II satellite missions that focus on the study of space weather effects involving the Earth's ionosphere and radiation belts. Adam has also spent summers working on the Hyperspectral Infrared Imager satellite (HyspIRI), an Earth Science decadal survey mission at Jet Propulsion Lab in Pasadena, California. Adam has published two papers regarding this mission: one on a concept for the missions high data rate communications system and another on how global cloud coverage will impact the missions science data.

## TABLE OF CONTENTS

1. INTRODUCTION .....	1
Space Weather .....	2
Problem Statement .....	4
EDSN Mission .....	6
2. BACKGROUND.....	9
Van Allen Radiation Belts .....	9
Particle Motion in the Belts.....	10
South Atlantic Anomaly.....	14
3. MOTIVATIONS .....	17
Related Work .....	17
Mission Objectives .....	20
Design Objectives .....	21
4. INSTRUMENT DESIGN .....	22
Detector Operation .....	22
Detector Characterization.....	27
Detector Calibration .....	32
Supporting Electronics .....	34
Software .....	35
Ground Support Equipment .....	37
5. ASSEMBLY AND TESTING .....	38
Fabrication .....	40
Instrument Testing.....	44
Safe-to-Mate Test .....	45
Acceptance Test .....	46
Performance Test .....	54
Test Analysis .....	55
Environmental Testing .....	59
High Altitude Balloon Flight.....	63
Satellite Integration and Testing .....	64
6. DATA COLLECTION.....	67

TABLE OF CONTENTS – CONTINUED

7. CONCLUSION .....	71
Lessons Learned.....	72
Future Work.....	73
REFERENCES.....	75
APPENDICES .....	78
APPENDIX A: Instrument Specifications .....	79

## LIST OF TABLES

Table		Page
1	Periods regarding the three fundamental motions of particles in the radiation belts: gyration, bounce, and drift [12].....	15
2	Densest materials in the spacecraft .....	31
3	Total stopping power along three chosen entry vectors. ....	32
4	Operating Specifications for the EPISEM Instrument based on test data from the 15 assembled units. ....	81

## LIST OF FIGURES

Figure		Page
1	Examples of events in the space weather affecting various technologies on and above the planet [43]. .....	3
2	Earth's inner and outer radiation belts depicted around the magnetic axis, image credit: NASA.....	5
3	Depiction of EDSN's star-type network topology with the lieutenants positioned around the captain, who is located in the center, image credit: NASA.....	7
4	Model of a single EDSN spacecraft. [11].....	8
5	Earth's inner and outer radiation belts as well as the northern auroral zone; the highest radiation or particle flux is shown in red, as simulated by the Air Force Research Lab. The orbits of a GPS and GEO satellites are shown for a sense of altitude [43].....	10
6	Earth's dipole field lines represented by L-Shell number (left), image credit: Creative Commons. True depiction of earth's magnetosphere against a bar magnet (right), image credit: NASA.....	11
7	Depiction of the three fundamental motions of particle groups in the radiation belts [7] .....	12
8	Particles motion along the L=1 magnetic field line located with its parallel ( $v_{\parallel}$ ) and perpendicular ( $v_{\perp}$ ) velocity components. ....	13
9	Depiction of the inner radiation belt precepitating below 500 km as what is known as the SAA (left). The area of this region shown on a map of the earth (right). The radiation flux is drawn as contour lines with the highest amount in the center [12]. ....	16
10	Figure depicting integral flux's of protons in the inner belt with energies >10 MeV (left) and electrons with energies >0.6 MeV (right), [10].....	18
11	Plot showing the correlation of electron energies across L-shells in the radiation belts, this shows that the belts are globally coherent across large spatial and temporal scales [18]. ....	19
12	Depiction of the spatial locations for the SAMPEX and POLAR satellites (left) and the proposed orbits for the EDSN constellation (right), orbital altitudes are not to scale. ....	19

## LIST OF FIGURES – CONTINUED

Figure		Page
13	Block diagram showing the primary circuits and components that make up the EPISEM instrument.....	23
14	Image of the EPISEM circuit board displaying the location of the primary circuits and components. ....	23
15	Monte-Carlo simulation of electron density near the tubes anode (left) [21], Depiction of a Townsend avalanche inside a Geiger tube (right), image credit: Doug Sim, CC BY-SA .....	24
16	Example of a negative going pulse produced by after a Geiger discharge as measured by an oscpe. ....	25
17	Muliple pulses from more than one Geiger discharge. Also shows the threshold level that can be set by the Amptek pulse amplifier discriminator. ....	26
18	Geometry used to calculate the throuput for a circular surface detector as it detects radiation from a point source.....	28
19	Cross-section of EDSN spacecraft shown without any solar panels. The three major particle entrace locations described in this analysis are shown in black. ....	30
20	Depiction of an ideal Geiger tube plateau curve, [21] .....	33
21	Block diagram showing the supporting electrons aboard the EPISEM instrument .....	35
22	Example of the Command and Telemetry program being used to run the EPISEM instrument. ....	36
23	Image showing the items making up the ground support equipment used to test the EPISEM instrument. ....	37
24	Flow chart showing the design, development, and fabrication of the EPISEM instrument. ....	38
25	Flow chart showing the initial bare board cleaning .....	41
26	Allowable degrees of freedom of the H1 assembly jig .....	42
27	Image showing process of board inspection and H1 installation after the boards were populated with most of components. ....	43

## LIST OF FIGURES – CONTINUED

Figure		Page
28	Depiction of the Geiger tube housing assembly and the soldering of the tube assembly onto the circuit board. ....	44
29	Image displaying the final staking, coating, and packaging process before the instruments were shipped to NASA. ....	45
30	Test points measured to ground in the power and unpowered portions of the Safe-to-Mate test. ....	46
31	Measured regulator switching waveforms (a and b) waveforms from datasheet (c) [45].....	47
32	Measured regulator ripple voltages (a,b,c,d) and datasheet ripple voltage (e) [45].....	48
33	In-rush currents during the instrument power on cycle.....	49
34	The 1 G $\Omega$ probe and multimeter used to take the truth measurement in the high voltage circuit monitor calibration, meter is currently reading 410V. The oscscope in the background is displaying an example of the HVPS ripple voltage, measured earlier. ....	50
35	Error in the high voltage monitor circuit for instrument number 21, before (left) and after calibration (right). ....	51
36	Width of pulse output from the Amptek A101 pulse amplifier discriminator as adjusted by an external capacitor C <sub>w</sub> [46]. ....	52
37	Example of the four plateau curves ran at each threshold setting during the Acceptance Test. ....	53
38	Example of plateau curves, the left curve trends upwards but this curve was still was considered a pass due to an optimal slope, right shows an example of a failed plateau curve.....	54
39	Three plots showing comparison of the results from tests regarding the instruments detector. across all 15 flight units.....	56
40	Two plots showing plateau curve comparisons across the 15 assembled and tested instruments. ....	57
41	Plots of percent deviation from the average in regards to values tested in the first Acceptance Test and last Performance Test ....	58
42	Setup and results from the thermal chamber test.....	60

## LIST OF FIGURES – CONTINUED

Figure		Page
43	Thermal vacuum chamber test setup showing the heating and cooling elements of the chamber along with where the EPISEM instrument was mounted.....	61
44	Thermal vacuum chamber temperature profile showing temperature dwell area and the location of Performace Tests .....	62
45	Thermal vacuum chamber temperature data as measured by external thermal couples and temperatures aboard the instrument .....	62
46	Plateau curves from the first cold (left) and hot (right) temperature plateaus during the thermal vacuum chamber test.....	63
47	Radiation measured by the instruments aboard the high altitude balloon flight in which EPISEM was tested on (left), image credit: BOREALIS Research Group MSU. Compared against the expected radiation environment from previous balloon flights (right) [23] .....	64
48	Integration an EPISEM instrument into the EDSN spacecraft electrical bus (left). Continuation of CubeSat stack integration by inserting threaded rods through the structural stand-offs (right) image credit: NASA.....	65
49	All fourteen of the fully assembled EDSN satellites (left). The eight flight units that will launch into space (right).....	65
50	Depiction of the eight EDSN spacecraft as they separate from the launch vehicle into two groups of four spacecraft each, after deployment into space. ....	67
51	Depiction of how the two groups of EDSN spacecraft separate with respect to the first spacecraft in the swarm (EDSN1) as simulated in Systems ToolKit (STK) from Analytical Graphics Inc .....	68
52	The ten minute periods (shown in yellow) that the instrument will be turned on once a day as simulated in STK .....	69
53	Average flux and electron microbursts in the radiation belts as measured by SAMPEX (left) [24]. Right is a cartoon of gross incoherence in the radiation belts along similar trajectory. ....	70
54	Depiction of the major angles of entry and their energy threshold for the non-uniform EDSN structure.....	80

## ABSTRACT

The ability to simultaneously monitor spatial and temporal variations in penetrating radiation above the atmosphere is important for understanding both the near Earth radiation environment and as input for developing more accurate space weather models. These models currently lack high resolution multi-point measurements to accurately portray the spatial and temporal variability of the radiation belts. To obtain data that may uncover the small-scale spatio-temporal variability of the areas around the planet known as the Van Allen Radiation Belts measurements must be made across a distributed array of satellites. The most recent decadal survey on solar and space physics states that the CubeSat platform is ideal for making these type of measurements [43]. The Energetic Particle Integrating Space Environment monitor instrument (EPISEM) will launch aboard eight CubeSat's as a part of the Edison Demonstration of Smallsat Networks (EDSN) mission. By being distributed across a geographically dispersed area, EPISEM will help fill the data gap by measuring the location and intensity of energetic charged particles simultaneously. This research describes the fabrication approach of the miniaturized radiation detection instrument aboard the EPISEM instrument and operational considerations unique to missions using many identical spacecraft and instruments. The EPISEM payload was specifically designed for CubeSats; leveraging heritage from the payload operating aboard Montana State University's Hiscock Radiation Belt Explorer (HRBE), launched in October 2011. The EDSN project is based at NASA's Ames Research Center, Moffett Field, California, and is funded by the Small Spacecraft Technology Program (SSTP) in NASA's Office of the Chief Technologist (OCT) at NASA Headquarters, Washington. The EDSN satellites are planned to fly late 2014 as secondary payloads on a DoD Operationally Responsive Space (ORS) mission that will launch into space from Kauai, Hawaii on a Super Strypi launch vehicle. The EPISEM payload was designed, built, tested, and delivered to NASA Ames by the Space Science and Engineering Laboratory at Montana State University.

## INTRODUCTION

Over the past twenty years the United States has become increasingly reliant on satellites and space-based technologies. These technologies, used by civilians and military alike, provide services such as: asset location via GPS, real-time satellite imagery, and a multitude of communications between many users. One major shift of technology to space is the fact that the airline industry and Federal Aviation Administration (FAA) is becoming a much heavier user of Global Positioning Systems (GPS). Preferring it over traditional ground based radars. This shift in direction to the use of more space-based assets comes with a much higher risk to infrastructure due to a lack of understanding of the space environment.

The environment above the Earth, where satellites and astronauts are located can be extremely hazardous. Sudden changes in this environment can cause hardware to become damaged or human lives to be placed in jeopardy. Both satellites such as the GPS constellation and the International Space Station (ISS) can be affected by these fluctuations in the Earth's ionosphere and radiation belts. The ISS' orbit is controlled enough to be kept away from the large amount of fluctuating radiation in the high latitude polar regions. Even it can be placed in danger when the belts become highly energized and grow to encompass lower latitude regions.

To better understand the effects of radiation on space-based assets, spacecraft engineers currently rely on physical models to assess the hazards the spacecraft will see on orbit. One of the most prevalent is the AE8/AP8 model used in predicting fluxes of high energy electrons (AE) and protons (AP). This model was first developed in the 1960s and has become one of the standards for representing an average of radiation a spacecraft may see on orbit. The problem with the AE8/AP8 and other models is that they tell nothing of daily or hourly particle fluxes; which may spike high

enough above the predicted mean to pose a serious threat to humans and spacecraft in orbit.

There is an updated version of AE8/AE8, the AE9/AP9 available to some U.S. government employees that does include many of these temporal changes. Though it is still limited to predicting radiation belt fluxes on larger spatial and temporal scales. Current spacecraft data only includes measurements involved with these macro-dynamics of the radiation belts [14][15]. Hence, the radiation belts are a major driver in a space weather system requiring further understanding by using smaller spacecraft to make more frequent measurements with increased spatial and temporal resolution. These measurements will provide much better predictive power for models and allow engineers and other decision makers to arrive at much better solutions regarding the survivability of space-based assets.

### Space Weather

Space weather is a blanket term used in describing the processes and interactions within the earth-sun system that is mainly driven by effects that take place outside our atmosphere. However, fluctuations in space weather does not solely effect space-based technologies, it also induces many changes here on earth. Figure 1 is a compilation of the ground and space based systems which are largely effected by the interaction between the earth's magnetic field and the solar wind. Space Weather has been known to not only damage satellites but has the ability to bring down power grids due to geomagnetically induced ground currents; cause large errors or disable GPS signals through scintillation; and even pose a risk to passengers and crew aboard planes with flight paths near the poles as well as astronauts orbiting the earth [39].

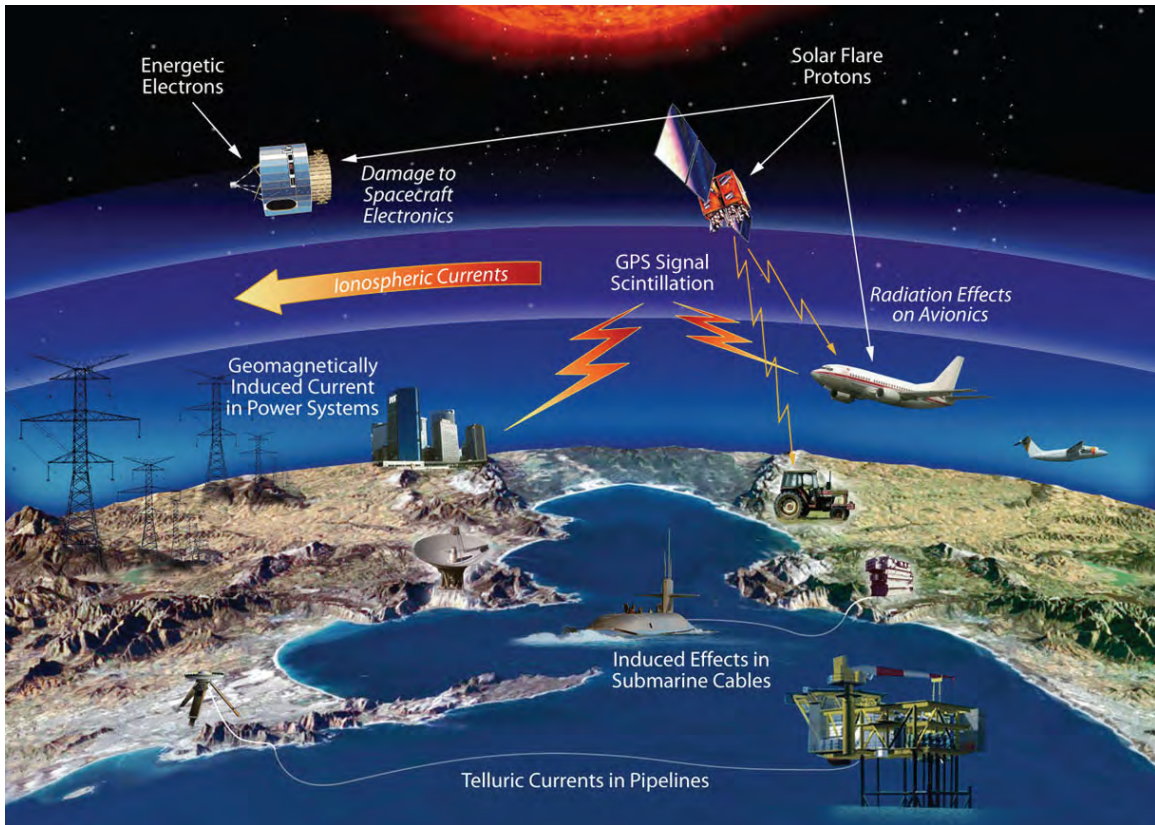


Figure 1: Examples of events in the space weather affecting various technologies on and above the planet [43].

High radiation zones in the near earth environment, known as the Van Allen Radiation Belts, are part of the planets space weather system that is even less understood than certain processes in terrestrial weather patterns. Predicting changes in these environments are done using physical models, such as AE8/AP8 or CREME, models which are data starved from lack of multi-point space-based measurements. As with the forecasting of terrestrial weather patterns, space-weather requires many different sensors taking constant data to detect real-time changes in the radiation belts, solar wind, as well as the ionosphere. To even truly understand the different processes in this system and how they interact, these measurements must be made with more than one instrument in different locations. The radiation belts by themselves are one

piece of the space weather system which will benefit from the mission and instrument described in this paper. The understanding of these belts' trapped energetic particles may also lead to much better forecasting of the overall space weather system and better data products for input into current models [43].

### Problem Statement

The radiation belts are a major aspect of the space weather system and encompass active regions around the Earth where relativistic particles become trapped by the planet's magnetic field. Figure 2 is a graphic of the regions which include both an inner and outer belt. Note that the closest they come to be with the earth is at the poles, these points are called the horns of the radiation belts. Once these particles are trapped they do not behave in any stationary manner but are subject to semi-stable adiabatic motions within the Earth's magnetosphere. The overall particle flux ( $\#$  particles  $\text{cm}^{-2}\text{s}^{-1}$ ) as they move is a topic of research focused on determining the short and long term dynamics of both the electrons and protons in these regions. The flux of these particles are both spatially and temporally variable which translates into fluctuations of the radiation belt size and particle density [43].

Particle flux variations have been previously studied with multi-satellite observations across large spatial distances and time scales on the order of tens of minutes to days [2][5][17][18][19]. These studies have shown that changes in belt particle populations display quite coherent behavior. Meaning that as particles enter the belts and become trapped they transition to an isotropic distribution with higher energy particles in the middle of the belt and lower energies toward the outer edges. This coherence suggests a global driving mechanism inside the earth's magnetosphere that energizes any incoming particles to conform to the same isotropic nature of

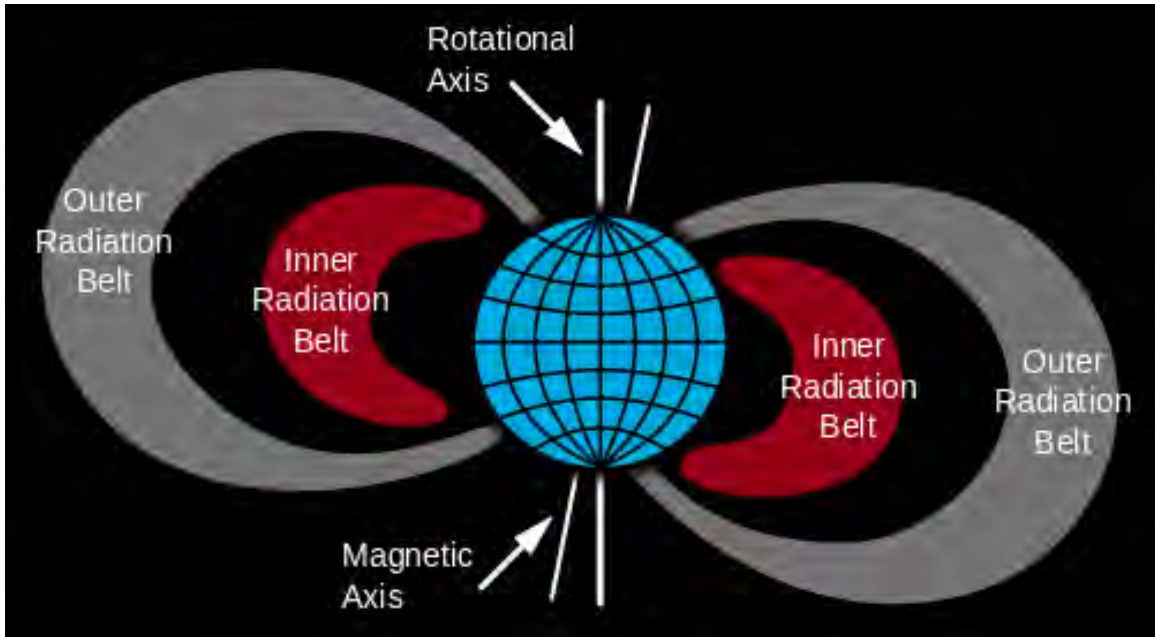


Figure 2: Earth's inner and outer radiation belts depicted around the magnetic axis, image credit: NASA.

those already in the belt. Previous studies have also shown that this isotropization occurs on timescales of half a day; which is a relatively slow process compared to the relativistic speeds of these particles.

These studies fall short in that the satellites collecting the data were distributed in orbits across a large spatial grid. And due to the normalized time between measurements, temporal resolutions were no better than ninety minutes. The impact of the large separations in space is that the overall spatial resolution of the measurements were limited to hundreds of thousands of kilometers. Additionally, due to the high variability of electron fluxes, a better determination of the isotropization time cannot be gleaned with the temporal resolutions from current spacecraft data.

This presents a need for a mission with satellites distributed across smaller spatial scales and shorter time intervals between measurements. Since a coherence has already been shown between low and high earth orbital altitudes, it leads to the ques-

tion of whether or not this behavior is present across smaller altitude distributions; in regards to both the electron heavy outer belt and the inner proton belt.

Understanding these fundamental particle dynamics and distributions through multi-point measurements will also lead to better forecasting models for space weather and the radiation belts. This enables not only a better protection of space-based technologies and the health of astronauts, but it will also further the knowledge of outer atmospheric and ionospheric conditions regarding other planets in the solar system. This understanding will help in the technological development needed to travel to these planetary bodies and beyond.

### EDSN Mission

The Edison Demonstration of Satellite Networks or EDSN mission which enables a multi-node measurement approach is a network of satellites being developed at NASA Ames Research Center, planned to launch late-2014. This satellite network consists of eight identical spacecraft which make up a star-type network topology where seven spacecraft are made “lieutenants” and one is made the “captain.” The hub or captain’s role is to receive and distribute commands from the ground station to the rest of the swarm while additionally acting as a focal point for all incoming data from each lieutenant. This architecture is shown in Figure 3 with the captain in the middle of the satellite swarm; receiving packets over a low data rate UHF link from each lieutenant and then downlinking that data to earth using the higher data rate S-band link.

In this topology, none of the lieutenants can be actively queried for data unless it is through the captain. But any lieutenant can switch roles with the current captain become the central hub if need-be. Though all lieutenants must pass their data through

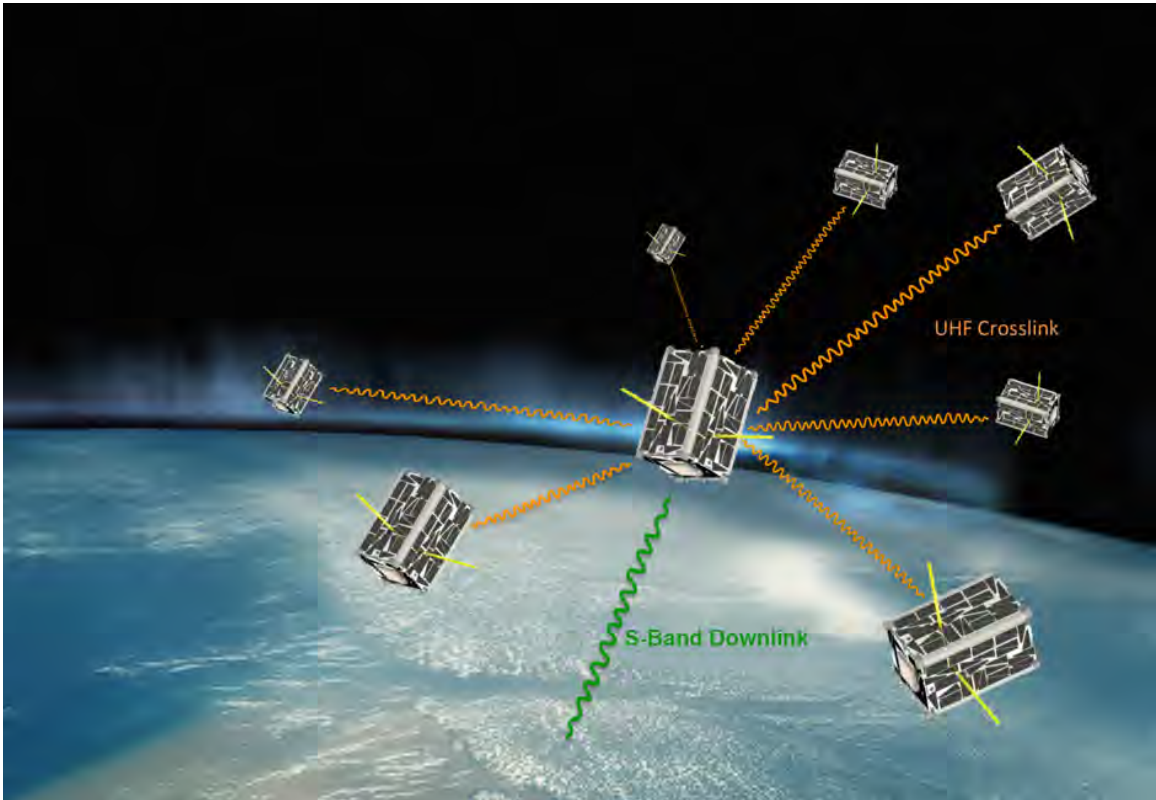


Figure 3: Depiction of EDSN’s star-type network topology with the lieutenants positioned around the captain, who is located in the center, image credit: NASA.

the captain, each spacecraft also includes a passive beacon that downlinks a subset the spacecrafts state-of-health and the science data from its EPISEM instrument as well.

The EDSN spacecraft bus that supports the EPISEM instrument (shown in Figure 4) are CubeSat form factor satellites [44]. They consist of a smartphone based flight computer, power system, GPS receiver, S-band and UHF radios, as well as an attitude control system which uses magnetic torque-coils and reaction wheels to actively stabilize the spacecraft. The swarm-like distribution of the eight EDSN spacecraft provides an ideal setting to help characterize radiation belt weather patterns by allowing simultaneous multi-point measurements to be collected across a small-scale spatially distributed array [11].

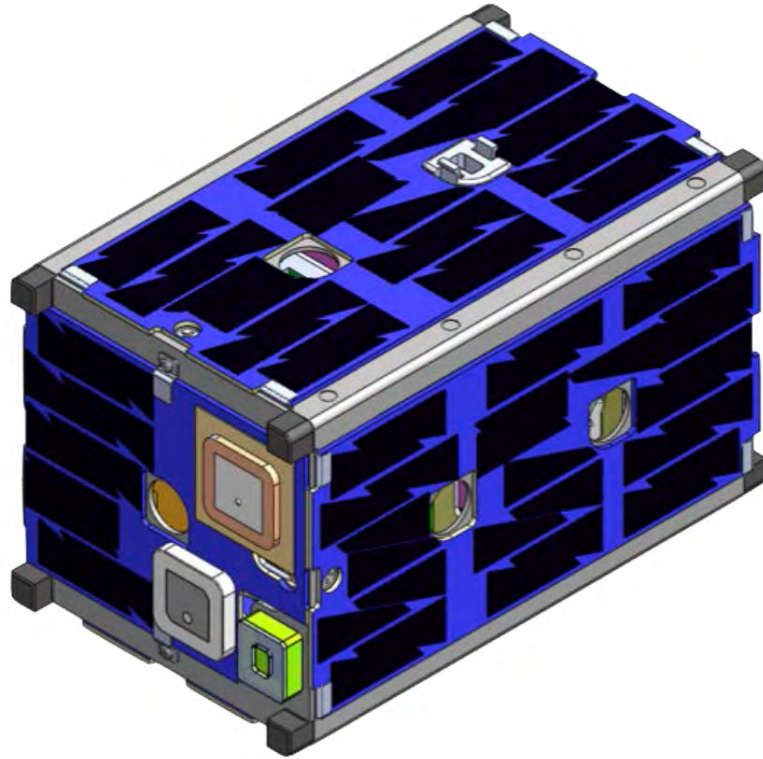


Figure 4: Model of a single EDSN spacecraft. [11].

Each EPISEM instrument receives unregulated battery power and enable commands from the spacecraft bus. When the EPISEM instrument is turned on it sends a data packet to the flight computer every 60 seconds. This packet contains the last sixty seconds of science data and current instrument state-of-health. A detailed description of instrument operations is discussed in Chapter 4. Once downlinked, the data taken by the EPISEM instrument in the EDSN array enables an unprecedented characterization of both spatial and temporal distribution regarding penetrating electrons and high energy protons.

## BACKGROUND

At the heart of the Space Weather system is the sun-earth connection. This connection is a complex process, driven by many different interactions. At the core of these processes is the interchange between the solar wind and the earth's magnetic field. This field prevents our planet's atmosphere from being stripped dry by deflecting much of the harmful radiation away from it. The deflection of radiation allows for a much more life inducing landscape on our planet. However in doing so, the magnetic field traps an amount of the radiation in the form of charged particles in belts around the earth. These congregation zones, are known as the Van Allen Radiation Belts. Once inside these belts, the particles motions are dictated by bounce, gyration, and drift dynamics as they move along "flux tubes" known as L-shells until disrupted.

### Van Allen Radiation Belts

The Van Allen radiation belts were discovered by James Van Allen in 1958 after the launch of America's first satellite: Explorer-1. These belts are toroidal-shaped regions that circle the earth's equator and are separately referred to as the inner and outer belt. The inner belt is located at mid-latitudes and expands from approximately 1.5 Earth radii to 4.5 Earth radii. This belt contains mostly energetic protons with energies  $>10$  MeV. The outer belt encompasses the inner belt and expands out to past 8 Earth radii. This belt contains energetic protons and electrons with energies  $>1.5$  MeV [22].

The image displayed Figure 54 depicts both the inner and outer radiation belt toroids with the orbit ellipses for both GPS and Geosynchronous Earth Orbiting (GEO) satellites. The satellite orbits provide an altitude reference as GPS satellites generally operate around 16,000 km where GEO satellites can be at altitudes above

35,000 km [41]. Note that neither orbit travels through the area of the highest radiation in the image. This image also shows a representation of the auroral oval where energetic particles can precipitate into the atmosphere causing the Aurora Borealis in the northern hemisphere and their southern hemisphere twin, the Aurora Australis [43].

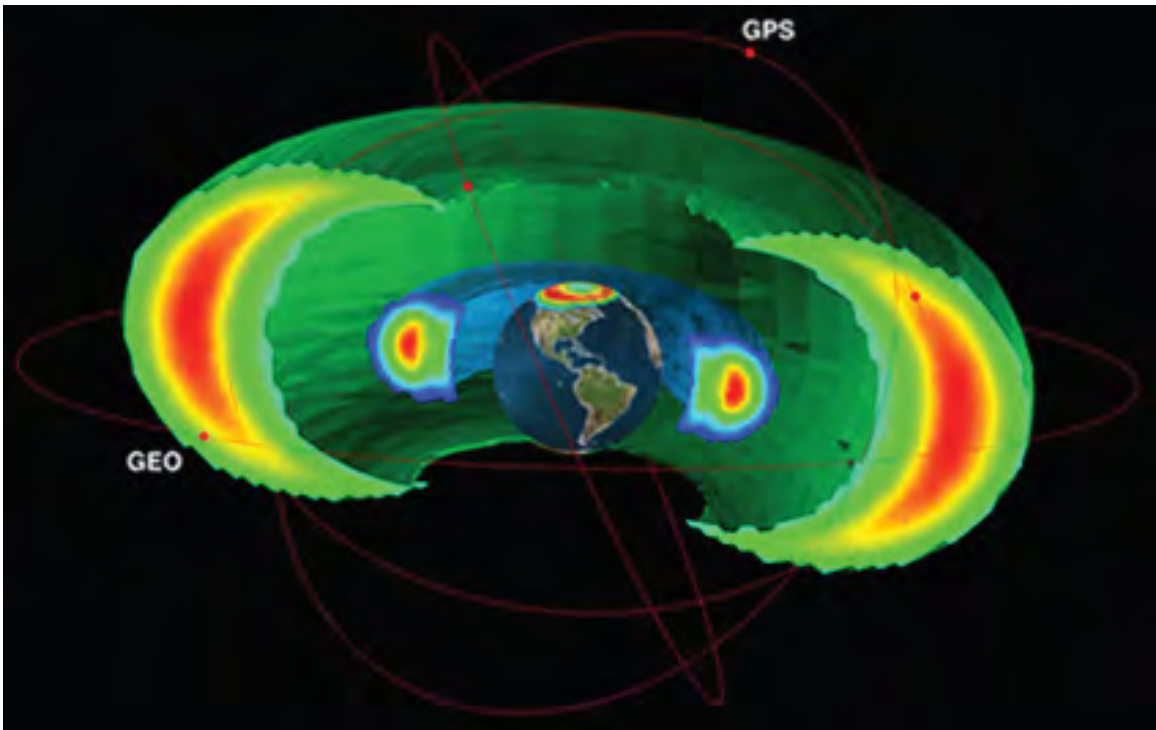


Figure 5: Earth's inner and outer radiation belts as well as the northern auroral zone; the highest radiation or particle flux is shown in red, as simulated by the Air Force Research Lab. The orbits of a GPS and GEO satellites are shown for a sense of altitude [43].

### Particle Motion in the Belts

Particle populations in the radiation belts are mostly high energy electrons, protons and heavy ions such as Helium. The majority of these particles originate from the sun and travel to earth on the solar wind, by flares or coronal mass ejections

(CMEs). Once the particles reach earth and become trapped they start to isotropize, exhibiting three fundamental types of motion along magnetic field line or L-shell.

The flux tubes or lines that particles travel along are normally described as L-shells [27]. This coordinate system was created to better describe the magnetic fields surrounding the earth which at low altitudes can be thought of as a dipole; though the further you get away from the earth the less and less this holds true. Figure 6 (left) shows the L-shell coordinate system with the earth represented as a dipole. L-shell values start at the earth's equator, which is  $L = 0$ , and expand outward in earth radii. The apex of the  $L = 1$  is one earth radii away from the surface of the earth at the equator. This coordinate system is extremely useful for describing locations in the radiation belts as they reside in and between L-shells.

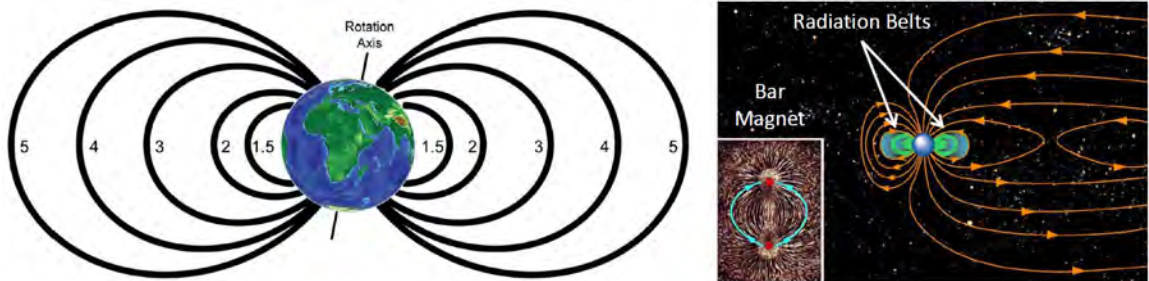


Figure 6: Earth's dipole field lines represented by L-Shell number (left), image credit: Creative Commons. True depiction of earth's magnetosphere against a bar magnet (right), image credit: NASA

This coordinate system is also useful when speaking to the earth's magnetosphere at distance much greater than five earth radii, when the magnetic field lines cease to look like a those of a bar magnet. Figure 6 (right) depicts earth's magnetosphere on a larger scale, this image shows compressed field lines on the side facing the sun and a long tail-like structure on the night-side of the planet. When referring to the

L-shells that represent field lines leaving the image in Figure 6 (right) their L-value increases exponentially to infinity.

The motions along an L-shell (shown in Figure 7) dictate that a trapped particle gyrates along a field line, bounces back and forth between the poles, whilst drifting longitudinally around the earth. These three fundamental motions, known as the adiabatic invariants, are constant, slow changing fluctuations that are conserved with respect to the particle. However, conservation of these motions is not always true. As these are only the dynamics used to describe particles trajectories over long time periods and across large spatial scales. Hence, a particles motion can change quickly in both a spatial and temporal manner with respect to an invariant. When a particle changes motion over a much shorter timescale than the overall adiabatic process it is said that the invariant is violated. An example of a violation can be best described with respect to a particles gyration and bounce invariant.

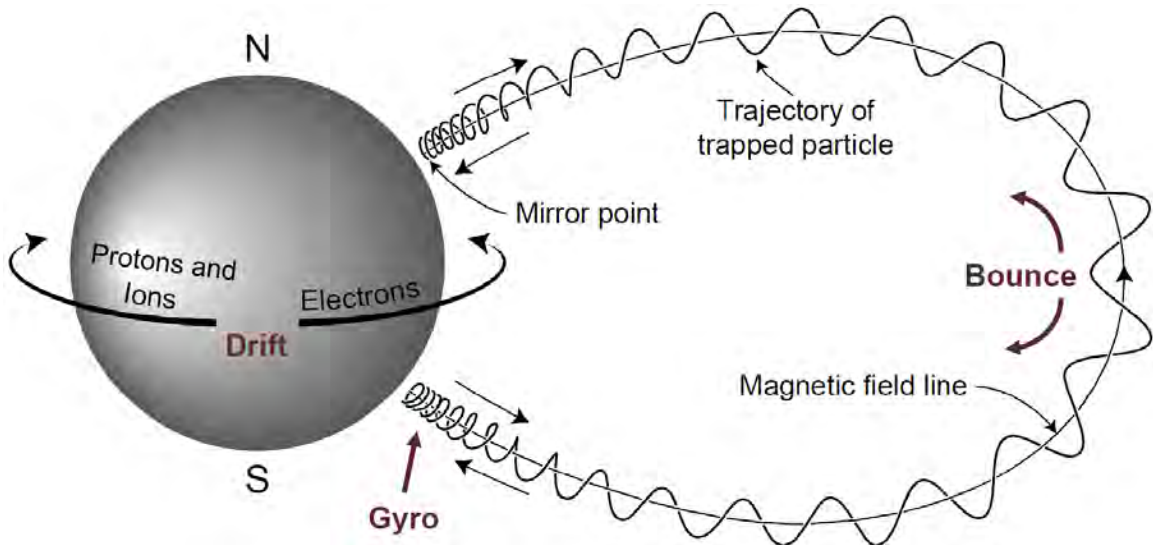


Figure 7: Depiction of the three fundamental motions of particle groups in the radiation belts [7]

As depicted in Figure 8 the gyro and bounce motion of a particle along one magnetic field line. This particle has an overall velocity that is made up of both perpendicular ( $v_{\perp}$ ) and parallel ( $v_{\parallel}$ ) velocity components. The arc-tangent of these components can be used describe the angular trajectory of the gyrating helix as it travels, this is known as the pitch angle ( $\alpha$ ) and is calculated by applying Equation 1. As the particle approaches a mirror point, its helicoidal velocity ( $v_{\perp}$ ) gets compressed and its parallel velocity goes to zero. When this occurs the particles pitch angle ( $\alpha$ ) becomes  $\pi/2$  ( $90^{\circ}$ ), as shown in Equation 2. The particle then reverses directions, continuing to its opposite mirror point [7].

$$\alpha = \tan^{-1} \left( \frac{v_{\perp}}{v_{\parallel}} \right) \quad (1)$$

$$\alpha = \lim_{v_{\parallel} \rightarrow 0^+} \tan^{-1} \left( \frac{v_{\perp}}{v_{\parallel}} \right) = \frac{\pi}{2} \quad (2)$$

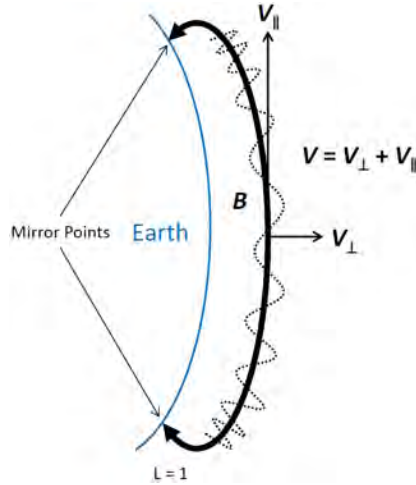


Figure 8: Particles motion along the L=1 magnetic field line located with its parallel ( $v_{\parallel}$ ) and perpendicular ( $v_{\perp}$ ) velocity components.

Since a particles perpendicular velocity component is made up of both its gyro-resonant frequency ( $\omega_g$ ) and a gyro-radius ( $r_g$ ) (related by Equation 3) an incoming

wave generated inside or outside the belts can interact with the particle in terms of its gyro-frequency. This interaction can cause its velocity component to change and therefore affect the particles perpendicular velocity. This would violate the gyro invariant allowing the particle to gain or loose energy and cause it to be “lost” or follow a new trajectory [7].

$$v_{\perp} = \omega_g r_g \quad (3)$$

Additionally, a particle traveling along a field line can precipitate (be “lost”) to a lower L-shell if its initial velocity components violate the bounce invariant or are changed through other interactions. Equation 4 shows a condition the particles velocity must meet in order to remain between two mirror points on a magnetic field line. If the ratio of the parallel to perpendicular velocities is less than the square root of the ratio of maximum ( $B_{max}$ ) to minimum ( $B_{min}$ ) magnetic field strengths the particle will experience a decreased bounce period or jump-to a lower L-shell.

$$\left| \frac{v_{\parallel}}{v_{\perp}} \right| < \sqrt{\frac{B_{max}}{B_{min}} - 1} \quad (4)$$

These three particle motions occur on timescales from milliseconds to minutes as shown in Table 1 [12]. Processes that cause the invariants to be violated occur on scales both shorter or longer. However, in a macro-sense it is believed that even though there are short time period dynamics in the belts, the overall changes in radiation flux are slow. Previous studies have shown this to be true, but again lack a distributed measurement.

### South Atlantic Anomaly

A special environment in the earth’s magnetosphere known as the South Atlantic Anomaly (SAA) is a weak spot in the earth’s magnetic field which contains high energy particles at a much lower altitude than elsewhere around the planet. Because of

Table 1: Periods regarding the three fundamental motions of particles in the radiation belts: gyration, bounce, and drift [12].

<b>Particle</b>	<b>Gyration Period</b>	<b>Bounce Period</b>	<b>Drift Period</b>
	(s)	(s)	(min)
10 MeV Protons at Low Altitude	$7 \times 10^{-3}$	0.65	3.0
10 MeV Protons at High Altitude	0.13	1.7	1.1
1 MeV Electrons at Low Altitude	$1 \times 10^{-5}$	0.10	10.0
1 MeV Electrons at High Altitude	$2 \times 10^{-4}$	0.30	3.5

the weaker magnetic field, particles mirroring along these L-shells have a much higher chance of precipitation from the inner belt to lower altitudes. Subsequently, this area poses a much higher risk to space based technologies as many of the assets orbiting the earth are located at these lower altitudes [20]. Spacecraft traveling through this area have a much higher probability of experiencing a single event effect, causing errors in their on-board electronics. Because all EDSN satellites and EPISSEM instruments are identical, taking measurements in this region may yield a better understanding of the specific environmental effects on spacecraft avionics. As one EDSN might have a fault in this region, where others may not.

The image shown in Figure 9 is a depiction of the inner radiation belt (left) as it precipitates to a lower altitude (500 km in this case). Figure 9 (right) shows the increased particle fluxes (in protons above 50 MeV per  $\text{cm}^2/\text{s}/\text{sr}$ ) at the South Atlantic region of the earth affected by the weakened magnetic field. Satellites passing through this region, at these altitudes, consistently experience hardware degradation and failures.

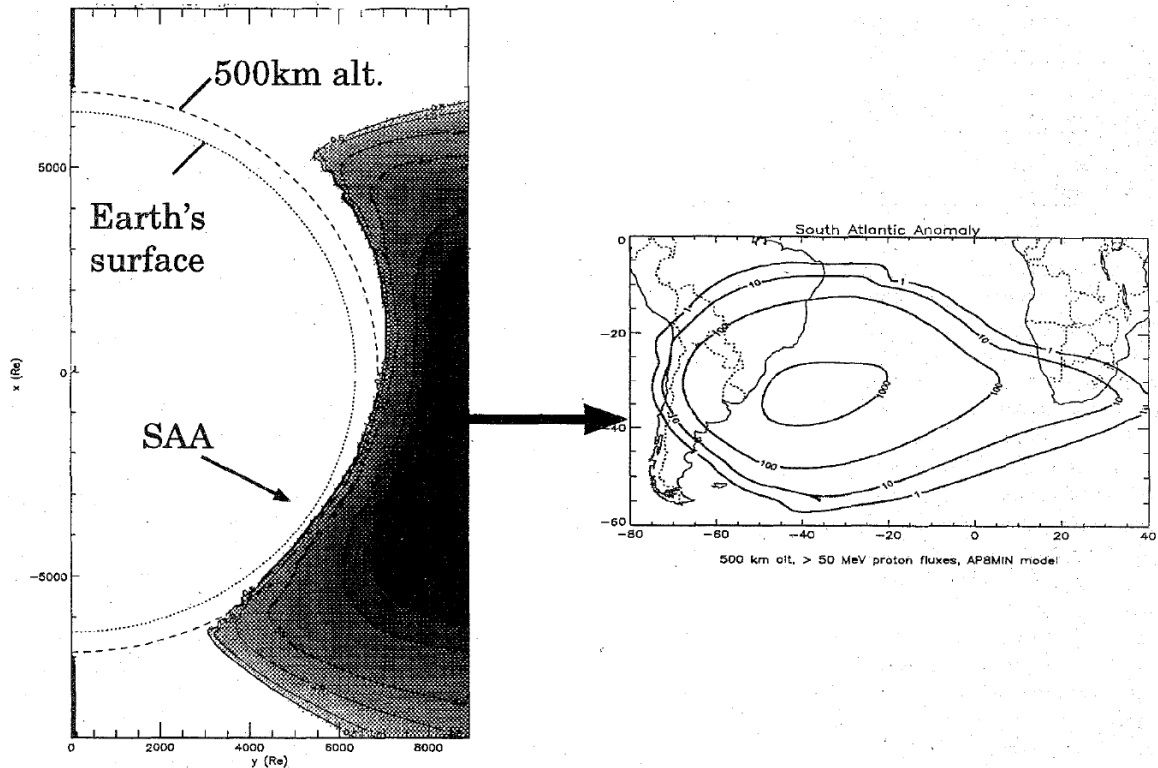


Figure 9: Depiction of the inner radiation belt precipitating below 500 km as what is known as the SAA (left). The area of this region shown on a map of the earth (right). The radiation flux is drawn as contour lines with the highest amount in the center [12].

Both the Van Allen Radiation Belts and South Atlantic Anomaly are important to understand as their content and dynamics drive many space weather phenomenon. Information gleaned from their study at fine spatial and temporal resolutions will provide the necessary inputs needed to better forecast space weather. The EPISEM instrument enabled by the EDSN satellite swarm will measure the environment of the radiation belts during its mission.

## MOTIVATIONS

The objectives of the EPISEM instrument are centered around answering the questions of spatial and temporal changes in the radiation belts that have been left open from previous studies. These studies have focused on long term changes in the radiation belts and have only been able to use measurements from satellites that had large distributions in both time and space.

### Related Work

Current radiation belt models describe particle fluxes as slow changing rates in both the outer electron belt and inner proton belt. Figure 10 is an example of an output from the AE8/AP8 model where a high concentration of radiation is shown in the middle of the contour, dropping off further from the center. The integral flux's represented in Figure 10 are protons in the inner belt with energies  $>10$  MeV (left) and electrons with energies  $>0.6$  MeV (right) [10].

This assumption of slow changing fluxes may not be true across the belts. As there are other, faster changing dynamics with respect to particle motion. These changes are not able to be properly detected with any current satellites as they are distributed across great distances. Localized pockets of high radiation zones may, under certain conditions, appear and disappear. At small scales these localizations may cause the belts to look much more scattered in their appearance than Figure 10 [12].

Over the long term and across large altitude ranges previous studies haven shown that changes in the particle flux rates are slow and associative across the entirety of the belts. One major study that was completed used data collected by the SAMPEX, POLAR, and the GOES satellites over a two year period [18]. The analysis method took the average flux measured by each satellite and related it in time. The results

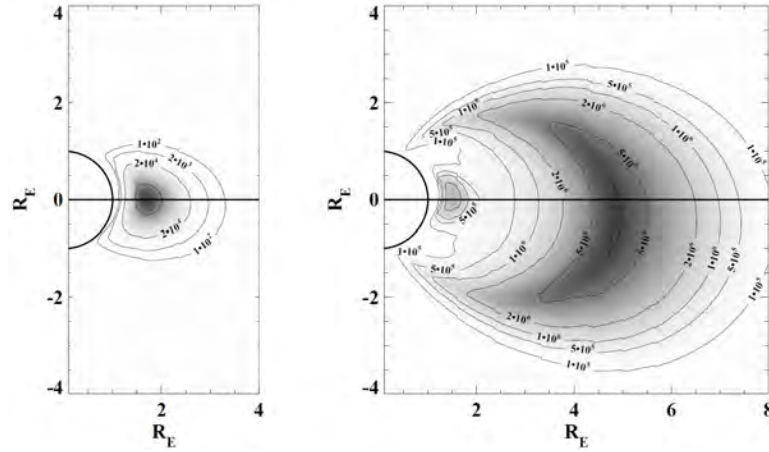


Figure 10: Figure depicting integral flux's of protons in the inner belt with energies  $>10$  MeV (left) and electrons with energies  $>0.6$  MeV (right), [10]

of the study show that the average radiation in the belts behaves quite coherently across the altitudes in which the satellites were located. Figure 11 shows a strong correlation in the measured electron flux between both SAMPEX and POLAR across L-shells when the lag time between measurements is less than a day. This coherence also suggests that violation of the adiabatic invariants, leading to long term changes in the radiation belts, happens on a global scale.

The shortcomings of this study were mainly due to different instruments aboard different satellites supplying the data. Because of this an overall time resolution of ninety minutes was the highest that could be achieved across all the satellites. This begs the question if the coherence holds at higher temporal resolutions. Additionally, since the satellites used to measure the electron fluxes were widely distributed it is also unknown if the spatial coherence holds the same across small altitude changes. Figure 12 (left) is a depiction of the spatial locations in which the POLAR and SAMPEX satellites were located. Figure 12 (right) shows a similar graphic of how the EDSN spacecraft will orbit the earth. The large difference between the two is that, upon deployment, the EDSN satellites will only be meters to kilometers apart and separate

slowly, where as POLAR and SAMPEX were more than tens of thousand kilometers apart, making it impossible to measure changes in flux at small spatial resolutions.

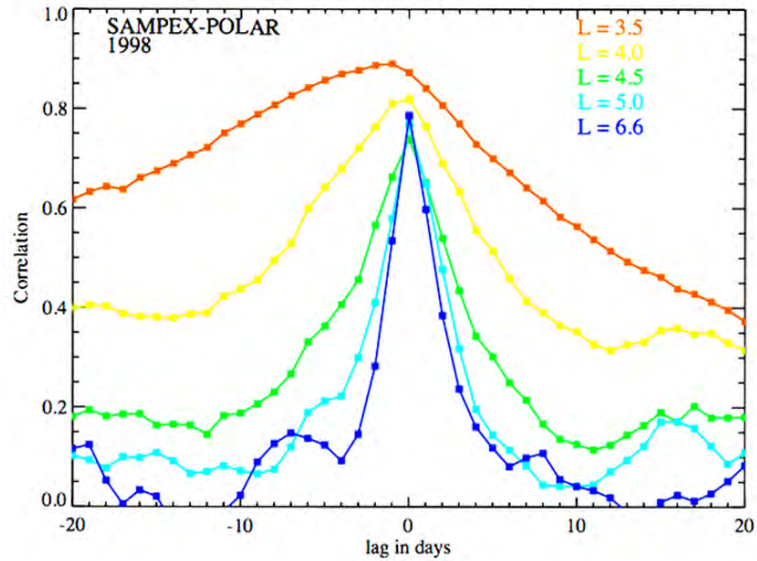


Figure 11: Plot showing the correlation of electron energies across L-shells in the radiation belts, this shows that the belts are globally coherent across large spatial and temporal scales [18].

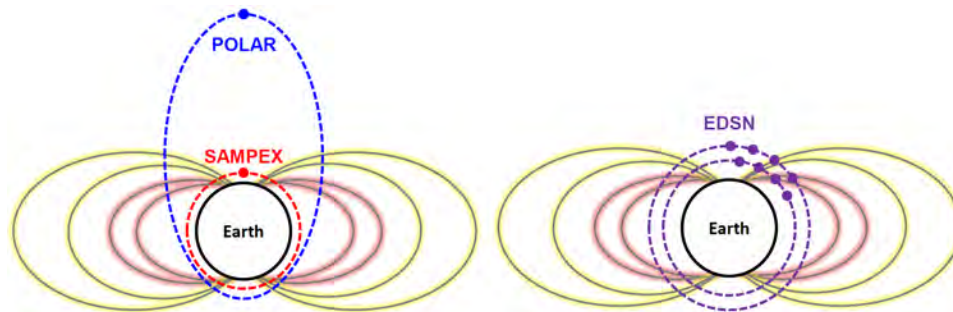


Figure 12: Depiction of the spatial locations for the SAMPEX and POLAR satellites (left) and the proposed orbits for the EDSN constellation (right), orbital altitudes are not to scale.

### Mission Objectives

As mentioned, the data gap lies in the fact that no measurements have been made on small spatio-temporal scales. The EPISEM instrument hopes to fill this by answering the primary science question:

- **How are the spatio-temporal distribution and temporal variability of penetrating electrons and high-energy protons characterized?**

Previous correlations show distributions that appear isotropic in nature across large spatial/temporal distributions, when lag time is less than one day. The measurements provided by EPISEM will measure flux rates on small spatial/temporal scales co-temporally across the EDSN array. These data will provide the first look of spatial coherence at these scales and temporal variations between successive measurements will characterize variations in intensity of more than an order of magnitude. Hence, the ability to characterize both spatial and temporal variations will allow them to be unraveled yielding much better knowledge about small scale dynamics in the radiation belts.

The secondary science question that the EPISEM instrument hopes to address is as follows:

- **What are the fundamental exposure rates of spacecraft avionics to radiation from penetrating electrons and high-energy protons in Low Earth Orbit?**

Since EPISEM provides constant radiation measurements for each identical spacecraft it will be able to measure the radiation environment when a single event effect or single event upset occurs in a spacecrafts avionics. Over the course of the EDSN

mission some spacecraft in the swarm may experience single event effects where others do not. This may be correlated to the radiation flux measured by each instrument. For example current models show that if all eight EDSN spacecraft fly through the South Atlantic Anomaly they all should be subjected to the same exposure rates. However, this may not be the case if the short-term dynamics of the anomaly cause large differences in these exposure rates.

### Design Objectives

In order to ensure that the mission objectives can be met and that the deviations in measured flux rates between each instrument are in fact due to the radiation environment and not nuances in the electronics themselves, all boards and detectors need to behave near identically. Because of this, much attention in the design process was spent to individually characterize each instruments electronics.

All eight flight instruments needed to also be identifiable on orbit, generate a low data volume, consume less than 80 mW of power, and operate without the need for any external protrusions or cut-outs in the spacecraft. The type of detector chosen for this instrument that best fits these requirements was a Geiger-Mueller particle counter. This detectors operation, characterization, and calibration are described in detail in Chapter 4.

Additionally, to properly meet the mission objectives the EDSN satellites needed to be distributed over small spatial scales and the location of the measurement must be known to within one kilometer. At a minimum measurements must be taken in the horns of radiation belts over all longitudes; as well as in the South Atlantic Anomaly. These requirements and the design solution are discussed further in Chapter 6.

## INSTRUMENT DESIGN

The functioning detector on EPISEM is a thin-walled Geiger-Mueller (GM) tube. This type of tube was chosen to make it easy to integrate the instrument into the CubeSat form factor where both internal and external satellite volume are highly constrained. The thin-walled tube type easily mounts to the center of the circuit board without needing any external windows or protrusions, allowing it to take up a minimum amount of internal volume. The remainder of the instrument board holds supporting electronics to enable the geiger tube, perform counting statistics, measure state of health, and packetize the data before sending it to the satellites flight computer.

A simplified block diagram is shown in Figure 13, describing the primary circuitry needed for operation of the EPISEM instrument. Operation of the detector and supporting electronics are discussed in the following sections. Figure 14 shows a picture of a fully assembled EPISEM circuit board with many of the primary circuits pointed out.

### Detector Operation

The Geiger tube is located in the center of the instrument circuit board which is ultimately housed at one end of the spacecrafts structure. The tubes anode has a capable operating range of 450 V to 650 V during normal operations it is kept at approximately 550 V, the middle of the range. This high voltage creates a strong electric field between the anode and the cathode of the tube. When an ionizing particle such as a high energy electron or proton penetrates the tubes thin wall it collides and therefor ionizes the neon fill gas, vacuum sealed inside the tube. The Neon's free electron is then accelerated to the anode by the electric field. As

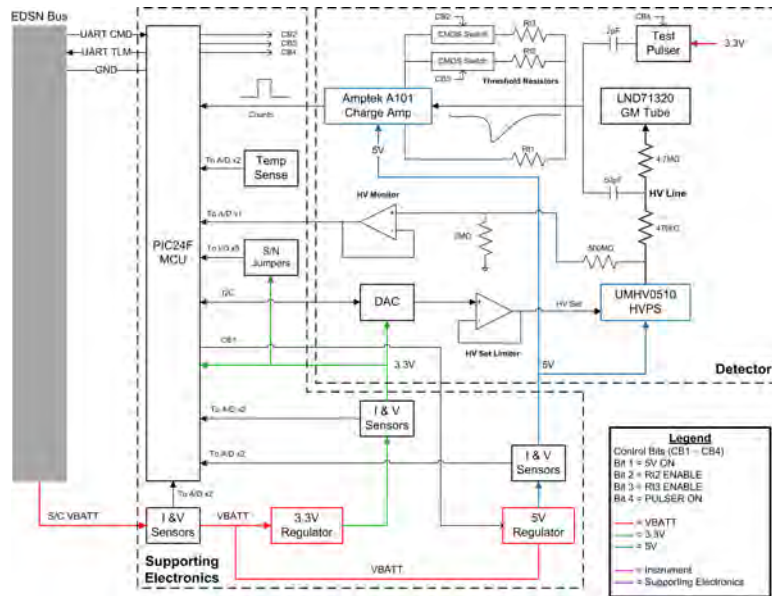


Figure 13: Block diagram showing the primary circuits and components that make up the EPISEM instrument.



Figure 14: Image of the EPISEM circuit board displaying the location of the primary circuits and components.

it is accelerated additional Neon ions are ionized, increasing overall electron density closer to the anode (Figure 15, left). The net effect from the initial ionizing particle is known as a Townsend avalanche, illustrated in Figure 15 (right).

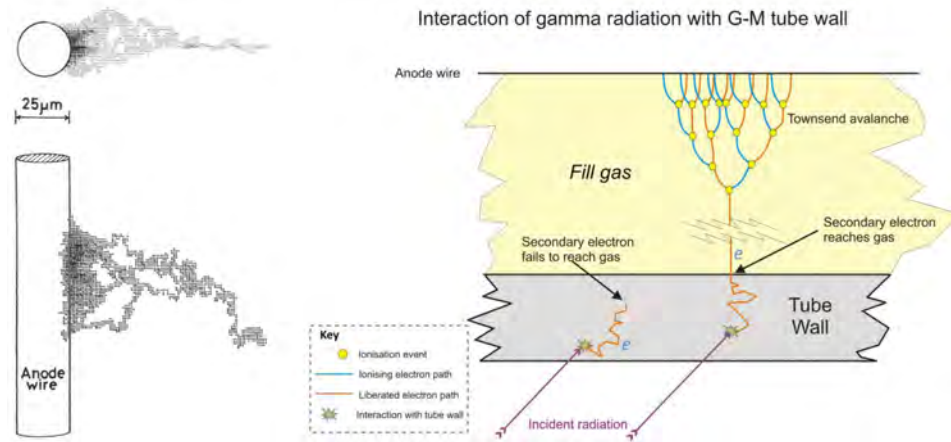


Figure 15: Monte-Carlo simulation of electron density near the tubes anode (left) [21], Depiction of a Townsend avalanche inside a Geiger tube (right), image credit: Doug Sim, CC BY-SA

As all the free electrons are accelerated towards the anode the less mobile positive ions begin to build up until they eventually reduce the strength of the electric field. This stops further avalanching and causes a Geiger discharge. The discharge is the electrons flowing out of the tube which produces a voltage spike or “pulse” across a quenching resistor soldered directly to the anode. The avalanche happens on the order of microseconds; after a particle penetrates the tubes aluminum wall and reaches the neon gas inside. The thin walled nature of EPISEM’s Geiger tube ensures that fewer incoming particles will be stopped by the tubes outer wall.

During an avalanche there is also a chance that ultra-violet (UV) wavelength photon’s can be created after an electron is knocked off its Neon atom. This may trigger additional avalanches and produce multiple pulses from one event. To remedy

this problem a small amount of quench gas is added that will absorb any UV photons, EPISEM's Geiger tube uses a Halogen as a quenching gas in this manner [21].

The discharge always occurs after the same density of positive ions are accumulated which causes the pulse to always be the same size; containing no information about the energy or particle species. Figure 16 shows a picture of a Geiger discharge pulse from one of the EPISEM Geiger tubes after it has been fully integrated onto the circuit board. The sharp edge on this pulse indicates that the tubes recovery time is mainly driven by tubes internal capacitance and not stray capacitance in the connection from the anode to the circuit board.

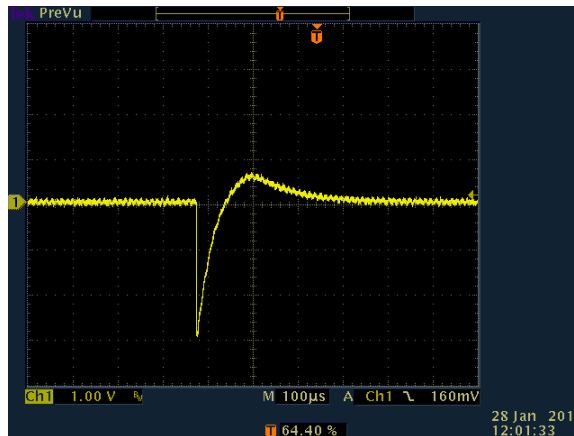


Figure 16: Example of a negative going pulse produced by after a Geiger discharge as measured by an osciopes.

The negative going Geiger pulse is next coupled through a low pass filter to remove the high voltage ripple seen in Figure 16. Then into a pulse amplifier discriminator (PAD) from Amptek which converts this spike to a transistor-to-transistor logic (TTL) pulse that can be counted by the instruments on-board microprocessor. The Amptek A101 is a commercially available radiation hardened amplifier that was chosen due to need for only one channel and that it has been used by SSEL on

previous missions. The A101 amplifier includes an adjustable output pulse width and resistor threshold setting, changing this threshold sets the voltage level in which the amplifier “counts” a pulse from the tube, less resistance equates to a lower threshold. This threshold feature was implemented by using CMOS switches and parallel resistor combinations to allow for an on-orbit adjustment. The resistance levels were calibrated by exciting a tube with a gamma source and stepping through a potentiometer connect to the A101’s threshold pins. This calibration was needed because too low a threshold results in the Amptek ignoring pulses from the tube that are close together.

An example of set threshold lines is shown in Figure 17, any pulse not exceeding the threshold is not counted by the A101. This figure also shows the recovery time of the detector when receiving multiple radiation strikes. Note that the minimum width between these pulses is approximately  $40 \mu\text{s}$ . This number corresponds to the manufacturers specified “dead-time” of  $45 \mu\text{s}$ .

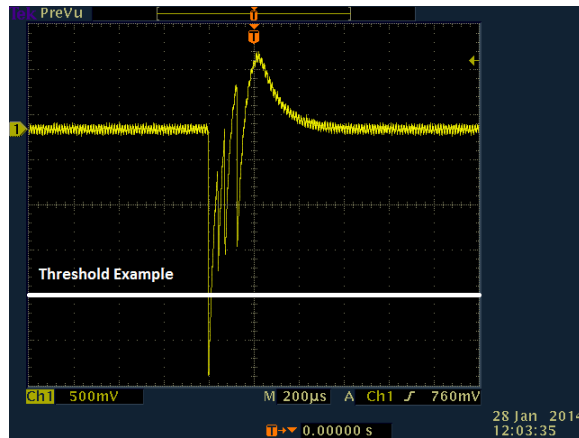


Figure 17: Multiple pulses from more than one Geiger discharge. Also shows the threshold level that can be set by the Amptek pulse amplifier discriminator.

### Detector Characterization

The Geiger tube particle detector aboard EPISEM, like all detectors must be characterized to properly interpret the data collected on orbit. First, the throughput or geometric factor of the detector was calculated. This number, in  $\text{cm}^2\text{sr}$ , represents how much of the particle population is being detected or “seen” by the tube in terms of the detectors geometry.

A detectors geometric factor is defined as the average projected solid angle of the detector subtended by its area and is found by integrating over all possible “look” directions that intersect with the detectors area. This factor is also known as the throughput or  $A\Omega$  product; where  $A$  represents the area of the detector and  $\omega$  its projected solid angle.

Figure 18 shows the geometry in circular surface detector system excited by a point source. Equation 5 is the resulting differential equation for this specific detector’s projected solid angle [21, p.118]. Integrating both sides of Equation 5 over all angles in a hemisphere ( $0^\circ$  to  $180^\circ$ ) results in a projected solid angle of  $\pi$  sr for a surface detector. This makes the geometric factor or throughput of a surface detector equal to its area multiplied by  $\pi$  [31][21][30].

$$d\Omega = \frac{dA \cos \theta}{R^2} \quad (5)$$

Due to the cylindrical nature of a Geiger tube detector, calculating its throughput is slightly different than that of a flat surface detector. In a the Geiger tubes case the surface area of the cylinder must be broken up into infinitesimally small surface elements and then integrated over all angles in a sphere [37]. The result is the basic formula for calculating the throughput of a Geiger tube, shown in Equation 6. Where  $a$  is the diameter and  $l$  is the length of the tube [34].

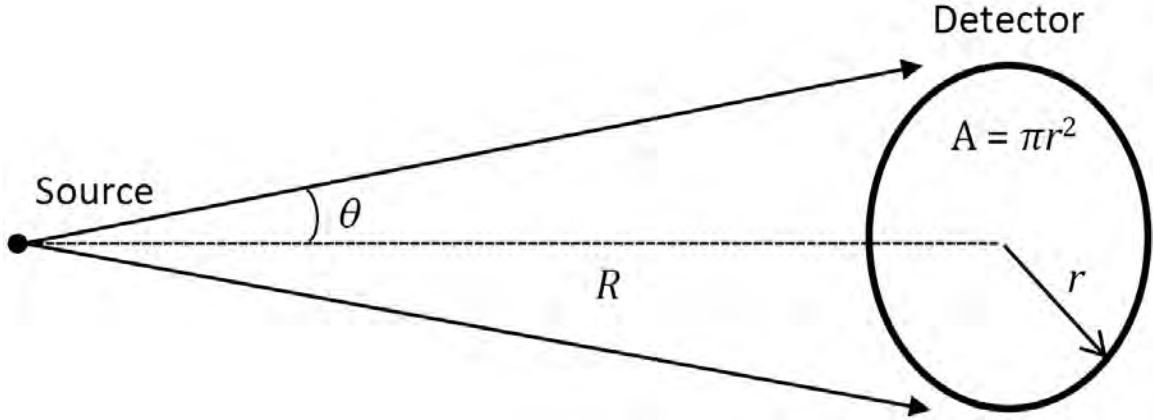


Figure 18: Geometry used to calculate the throughput for a circular surface detector as it detects radiation from a point source.

$$A\Omega = \frac{\pi}{4}al(1 + a/2l) \quad (6)$$

The LND71230 Geiger tubes on each EPISEM instrument have the dimensions of  $a = 0.777$  cm and  $l = 2.790$  cm, making the throughput of these tube  $1.94$  cm<sup>2</sup>sr. For comparison the Geiger tubes aboard the Explorer-1 mission that first discovered the radiation belts had the dimensions of  $a = 1.984$  cm and  $l = 10.160$  cm; yielding a much larger throughput:  $17.4$  cm<sup>2</sup>sr [34]. Even though the EPISEM tubes have a smaller collection area, this does not take away from the measurement of omnidirectional particle flux in the same radiation environment as the original Van Allen experiment. The number of counts “seen” by the EPISEM tube will simply be much less than the counts seen by the Explorer-1 Geiger tube, scaled down by almost an order of magnitude due to the difference in throughputs.

The omnidirectional intensity or particle flux ( $J$ ) for the EPISEM detector can be finally found by taking the instruments measured count rate ( $N$ , in counts/sec), dividing it by the throughput ( $A\Omega$ ), and multiplying by a count efficiency scaling factor ( $\epsilon$ ) or the number of counts recorded divided by the number of radiation quanta

incident on the detector. Applying this equation, shown in Equation 7, results in properly scaled counting statistics as measured by the detector [34].

$$\frac{N}{\epsilon A \Omega} = J \text{ in counts per m}^{-2}\text{sec}^{-1}\text{sr}^{-1} \quad (7)$$

Another part of this detector system that needs to be accounted for is the fact that the Geiger tube doesn't differentiate particle species. The tube effectively acts as an particle integrator, reporting the integral flux of its environment above a certain particle energy threshold. If this tube were free floating in space its threshold would be solely driven by the thin aluminum wall separating the gas and anode from the outside environment. However, the EPISEM instrument resides in a CubeSat structure with different obstructions visible to different parts of the cylindrical detector. The non-uniformity makes it difficult to back out the overall integral flux that will be measured by this instrument, though it can be approximated.

The image displayed in Figure 19 shows the location of the EPISEM instrument board in the EDSN CubeSat bus. Because the Geiger tube detector's geometric or view factor is practically a sphere, every obstruction in a particles path from outside of the structure to the tube will effect the threshold energy of the particles in which it detects. To find the threshold energy for the EPISEM instrument the Continuous Slowing Down Approximation (CSDA) was applied [9].

The CSDA method first approximates all particle paths to their average length traveled and assumes the rate of energy loss through this path is equal to the total stopping power of the obstructions through which the particle travels. Table 4 shows the materials with the most stopping power that the particles must travel through. Copper refers to the copper pours in printed circuit boards, it was assumed that all circuit boards in the spacecraft had three full layers of copper approximately 0.11 cm thick. The batteries in the spacecraft are standard lithium-ion 18650's, these



Figure 19: Cross-section of EDSN spacecraft shown without any solar panels. The three major particle entrance locations described in this analysis are shown in black.

batteries are 1.86 cm thick and made up of multiple elements whose average density is  $2.54 \text{ g/cm}^2$ . Next, the aluminum shielding category includes any radio frequency or other shields used to protect the circuits from electro-magnetic interference. All aluminum shields in the spacecraft were assumed to be 0.1 cm thick. The final material that all particles must travel through before reaching the gas-filled portion of the detector is the aluminum tube wall, the thickness of this wall is also shown in Table 4. The CSDA is calculated by taking the density of the material and multiplying it by the total thickness of the material in the spacecraft. From this CSDA range the maximum energy of protons and electrons stopped by the material was calculated by using the National Institute of Standards and Technology's ESTAR (stopping power for electrons) and PSTAR (stopping power for protons) tables [9].

Table 2: Densest materials in the spacecraft

<b>Material</b>	<b>Density</b> (g/cm <sup>3</sup> )	<b>Thickness</b> (cm)	<b>CSDA</b> (g/cm <sup>2</sup> )	<b>Electrons</b> (MeV)	<b>Protons</b> (MeV)
Copper	8.96	0.114	1.02	2.0	25
Batteries	2.54	0.114	1.02	8.0	60
Aluminum Shielding	2.70	0.100	0.270	4.5	13
Steel Tube Wall	7.80	0.005	0.039	1.5	3.5

Referencing Figure 19 particle entry was simplified to three major non-uniform entrance vectors: top, bottom, and side. The thickness of the three densest materials was then added up and the CSDA calculated. This along with the resulting maximum energies of protons and electrons stopped along the three major entrance vectors is shown in Table 3. Again, referencing the CSDA, the total stopping power along these entrance vectors is equal to the maximum stopping power of the densest material. This means that entry through the top of the spacecraft has the most stopping power due to the particles having to travel through many layers of copper. Only electrons above 20 MeV and protons above 95 MeV will penetrate enough material to reach the detector. However, even though the top-entry vector has the most stopping power, the reality is that the bottom and sides encompass more areas of entry overall. Therefore, using the approximation data, all electrons above 3 – 5 MeV and protons above 35 – 45 MeV will likely be detected by the Geiger tube. The major angles of entry and their energy thresholds are shown in Appendix ??.

Though this is a useful approximation to know when producing a final data product, it is only an approximation. The true method of determining the energy bound above which the Geiger tube will integrate is to run an analysis using the space-

Table 3: Total stopping power along three chosen entry vectors.

Particle Entry	Material	Layers	Electrons Stopped	Protons Stopped
			(MeV)	(MeV)
Top	Copper	10	20.0	95.0
	Aluminum	5	1.75	27.5
	Batteries	1	8.00	60.0
	Steel	1	1.5	3.5
Bottom	Copper	2	3.0	35.0
	Aluminum	3	1.0	20
	Steel	1	1.5	3.5
Side	Copper	1	2.0	25.0
	Aluminum	1	0.60	12.5
	Steel	1	1.5	3.5

craft solid model with the “Geant4” toolkit or something similar. This toolkit using a Monte-Carlo type method to trace many different particle paths and produces a truer idea of the energies of protons and electrons that will be stopped. Additionally, because the EDSN spacecraft bus will provide no pointing knowledge with regards to the detectors measurements the only interest is an average stopping power over all entrance vectors.

### Detector Calibration

Though all detectors are the same in terms of geometry and placement inside the satellites, each Geiger tube behaves slightly differently as they cannot be manufactured with zero variation. These differences also need to be characterized and calibrated to ensure that the tube hasn’t degraded and is still operating in the plateau

region. Calibration is done by exciting the tube with a source at a fixed distance away and stepping through its operating voltage range. The result is a sharp ramp up when the tube turns on followed by a plateau, if the plateau slope is too great the tube may be showing signs of degradation and cannot be trusted to provide proper data. Figure 20 is an example of an ideal plateau curve, Chapter 5 describes in further detail the process in which each instruments Geiger tube detector was testing.

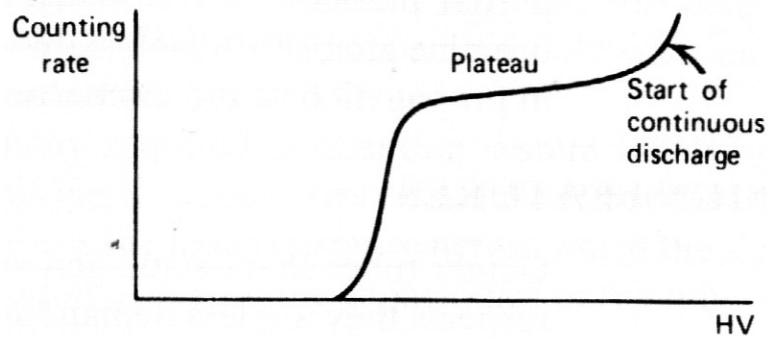


Figure 20: Depiction of an ideal Geiger tube plateau curve, [21]

The additional electronics that make up the detector portion of the instrument ensure that both the Geiger tube is and amplifier are operating properly. A high voltage limiter, voltage monitor and test pulser circuits were included in these electronics (as shown above in Figure 13). The voltage limiter circuit is an essential circuit, protecting the Geiger tube from potential damage by limiting the maximum value that the High Voltage Power Supply (HVPS) can be set to. This hard limit was set by tuning the maximum gain on a non-inverting operational amplifier (op-amp) to be well below the HVPS's maximum output of 1000 V. This circuits op-amp also allowed proper current to be sourced to the HVPS's "High Voltage Set" pin which the Digital-to-Analog Converter (DAC) was incapable of providing.

Subsequently, the high voltage monitor measures the voltage being output to the Geiger tube so that if the power supply is operating at a level far above or below 550 V it can be known as this measurement is taken once every minute or each time a group of sixty samples of count data from the tube is accrued. Finally, the Test Pulser circuit was included in the instrument design to bypass the tube and provide a reference count rate of 1000 counts per second. This can be ran in the lab or on orbit without the need for a radiation source and ensures that all the electronics and software post Geiger tube are functioning properly.

### Supporting Electronics

The instruments supporting electronics (Figure 21) ensure proper detector power, data collection, state-of-health, and instrument safety. At the center of this section is the PIC24F Microcontroller Unit (MCU). This micro is enabled when the spacecraft bus sends battery voltage to the instrument. Once turned-on EPISEM's 3.3 V regulator sends its output voltage to the PIC24F. At this stage the microcontroller starts collecting all available state-of-health data and waits for a command from the EDSN spacecraft bus.

To set the EPISEM instrument into a nominal data collection state the satellite bus needs to send a set of commands over the UART connection. These commands include enabling the 5.0 V regulator and setting the high voltage power supply to 550 V. Optional commands include changing the A101's threshold setting or enabling the test pulser.

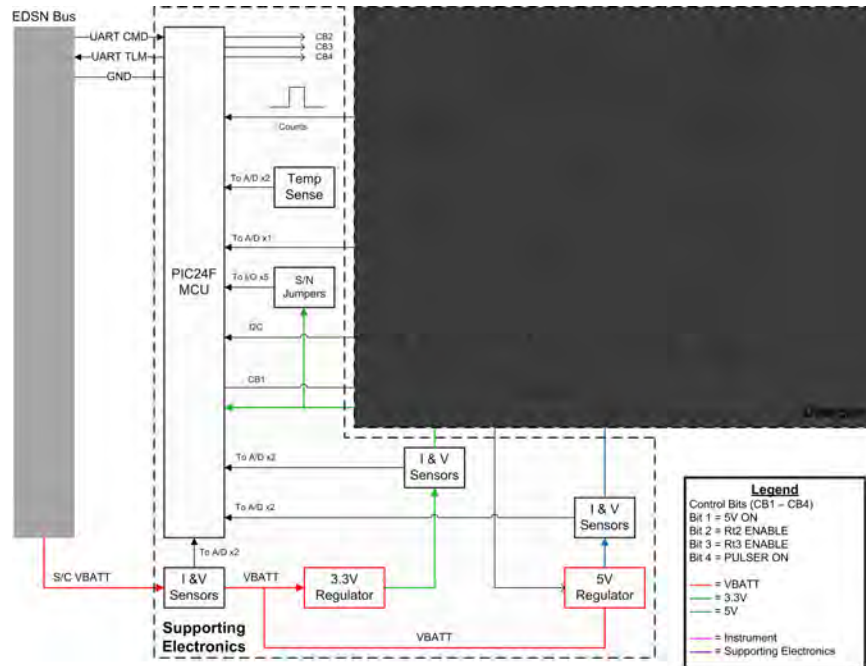


Figure 21: Block diagram showing the supporting electronics aboard the EPISEM instrument

## Software

The two integral pieces of software needed to test and run the EPISEM instrument were the flight software running on the PIC24F microcontroller and the a C# program used to test the instruments on the ground. Both programs were written by Matthew Handley and revised after running the Acceptance Test on the first revisions of the instrument. The C# Command and Telemetry (C&T) software program was a custom Graphic User Interface (GUI) that had the capability to both run automated test scripts and log measured values. This feature greatly reduced the amount of time needed to not only run the Acceptance Test procedure but the Performance Test as well. This software can also produce real-time plots which were very important for environmental testing.

An example of C&T software receiving real-time telemetry from the EPISEM instrument is shown in Figure 22. This image displays the raw packet values in hexadecimal (left), housekeeping data (middle), and the science data in counts per second (right). Note that the test pulser is being exercised during this test as the high voltage is turned off and the science counter data reading approximately 1000 counts/sec<sup>1</sup>.

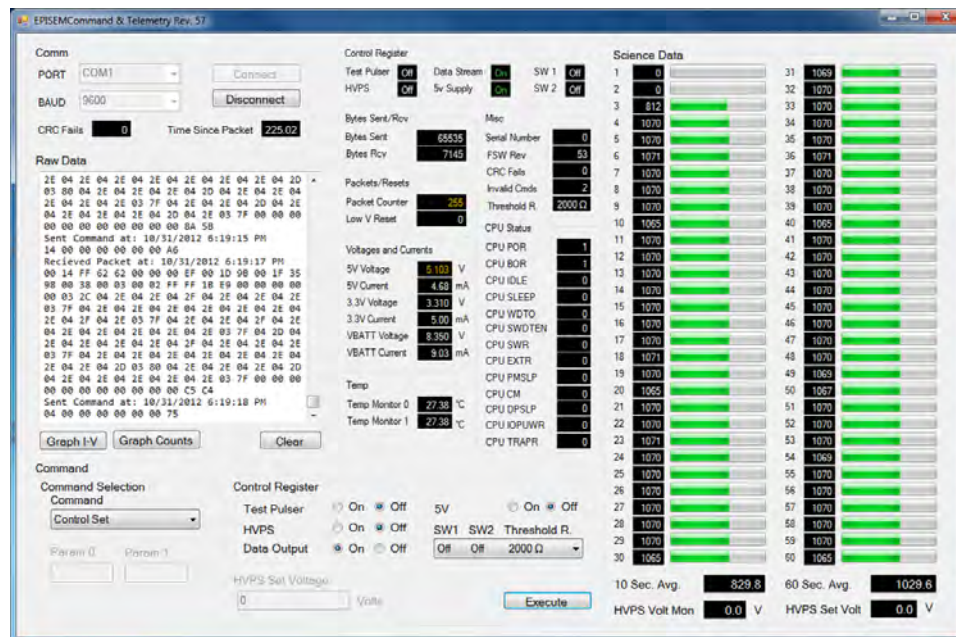


Figure 22: Example of the Command and Telemetry program being used to run the EPISEM instrument.

<sup>1</sup>All the software for the EPISEM mission was designed and written by Matthew Handley, an undergraduate computer engineer at Montana State University

### Ground Support Equipment

The ground support equipment or GSE for the EPISEM project was very minimal and included a test stand that doubled as a storage container and safe shipping container for each instrument. Other GSE includes a radiation source holder, testing cable for powering the circuit board and receiving telemetry through a computers USB or COM port. Additionally, as well as a programming cable was employed to upload the instruments flight software. Figure 23 shows a standard GSE setup minus the lid for the test stand which is used to protect the instrument during shipping and storage.

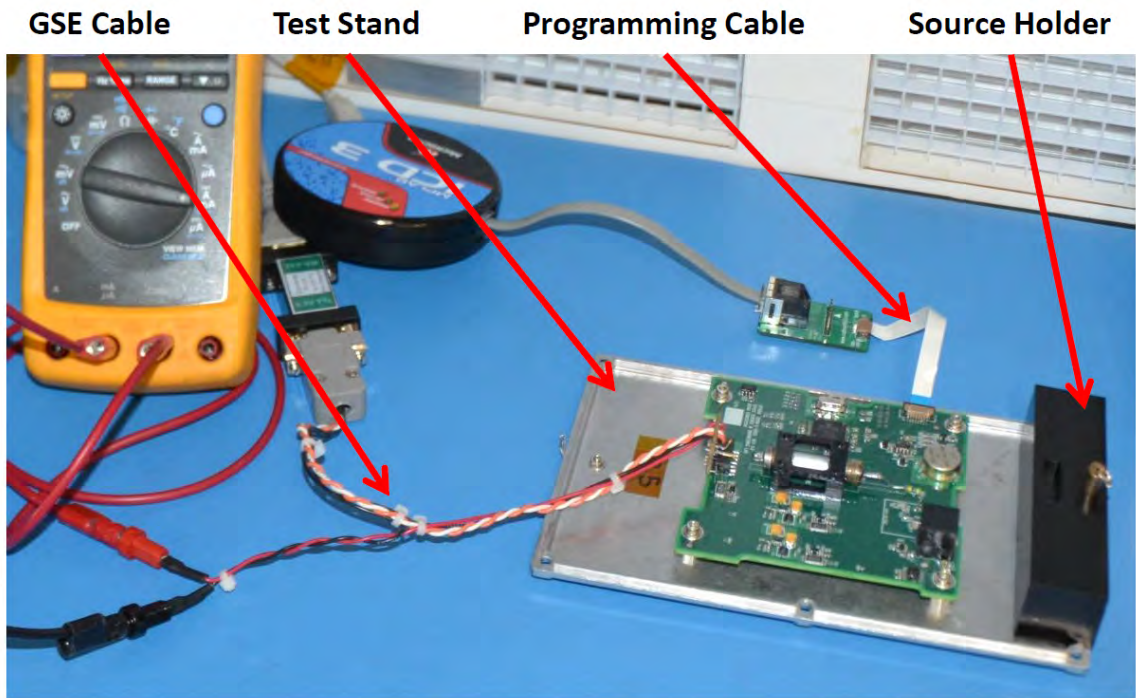


Figure 23: Image showing the items making up the ground support equipment used to test the EPISEM instrument.

## ASSEMBLY AND TESTING

A depiction of the iterative design process from the initial or prototype design phase to final flight fabrication, assembly, and testing is shown in Figure 24 below. The EPISEM instrument went through a total of four design revisions, the first two were during the prototype phase and last two were during the flight fabrication phase. The prototype phase involved short production runs in which only one board was populated and tested. During each of these revisions (1.0 and 2.0) an Acceptance Test was drafted, ran, and revised with the tests that were deemed important. This test document reflected the official log during the early design phases before being finalized for use in the flight unit testing phase.

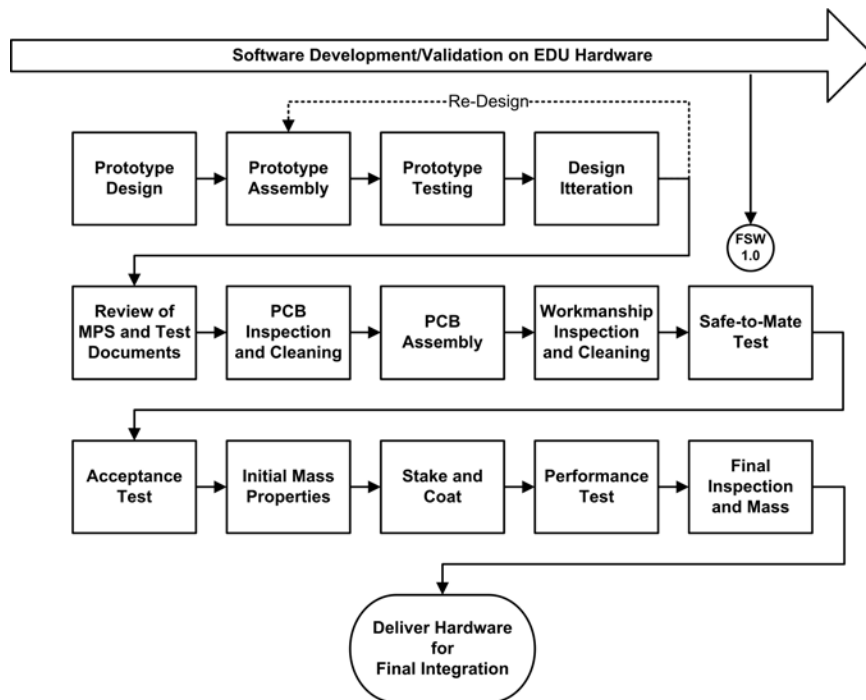


Figure 24: Flow chart showing the design, development, and fabrication of the EPISEM instrument.

During the testing of the first prototype revision it was revealed that the board drew too much power and had a lot of noise present on the current sensors. The second prototype included scaled down regulators and added low pass filters on each current sensor, with a corner frequency designed to approximately 1.6 kHz. Testing on the second revision showed that the design was ready for flight production. With minor changes to the layout and schematic revision 3.0, was sent out to be fabricated.

After the revision 3.0 boards were received and the fabrication process completed up to installation of the detector; it was discovered that there was a 9 mm error in a mechanical cutout with all the revision 3.0 boards. The mechanical specifications provided in the instrument-to-spacecraft interface control document (ICD) listed tolerance on these cutouts to be within  $\pm 0.1$  mm. Because all revision 3.0 boards were in violation of this tolerance they would not be able to be integrated into the spacecraft designed by NASA Ames'.

Upon a failure review board and subsequent write-up of a Non-conformance Report it was discovered that this error was due to a misplaced negative sign in the location of the cutout from the origin in the circuit board layout program. The CAD file provided to NASA Ames for mechanical checkout did not have this error. A drastic misrepresentation that was part user error and partly due to the circuit design programs poor ability to export properly scaled drawings for import into mechanical design programs such as SolidWorks. When SolidWorks was used, the board cutout was re-created from the ICD and not the actual design that would be fabricated at the board shop. More of this topic will be discussed in Chapter 7 under lessons learned.

### Fabrication

The first part of the flight fabrication phase was to send out the CAM or GERBER files to the board shop so they could fabricate the PCB substrates. During this week of down time the following four documents were prepared for each of the fifteen boards: a Manufacturing Planning Sheet (MPS), Safe-to-Mate Test Procedure, Acceptance Test Procedure, and Performance Test Procedure. Each document was serialized to its individual boards hardware coded serial number. At the end of the Assembly and Testing phase the completed documents would be scanned into a PDF and packaged with its board's shipment to NASA, on a CD. Any inspection notes, non-conformance, re-work, or other important information during the entire fabrication process was logged and captured on each boards MPS.

Once the circuit boards were received from the board manufacturer they are first soaked in an ethanol bath, scrubbed with a horsehair brush in a second ethanol bath, dried with nitrogen, baked out for eight hours at 60 °C, inspected, and double ESD bagged. This process, illustrated in Figure 25, ensured the best 15 out of the 25 boards would be sent out to be populated and that all boards were clean of any oils before sending them out for component placement.

After all flight boards were inspected they were sent out to be populated with all but a few components: the Geiger tube, quenching resistor, and spacecraft electrical bus connector (H1). A single flight board was first populated and sent back to MSU, fully assembled and tested to confirm there are no issues with the design before populating the rest of the boards. Upon receipt of all the flight boards, save the previously assembled unit, each board is inspected and cleaned again in an double ethanol bath, removing all stickers in preparation for the installation of H1.

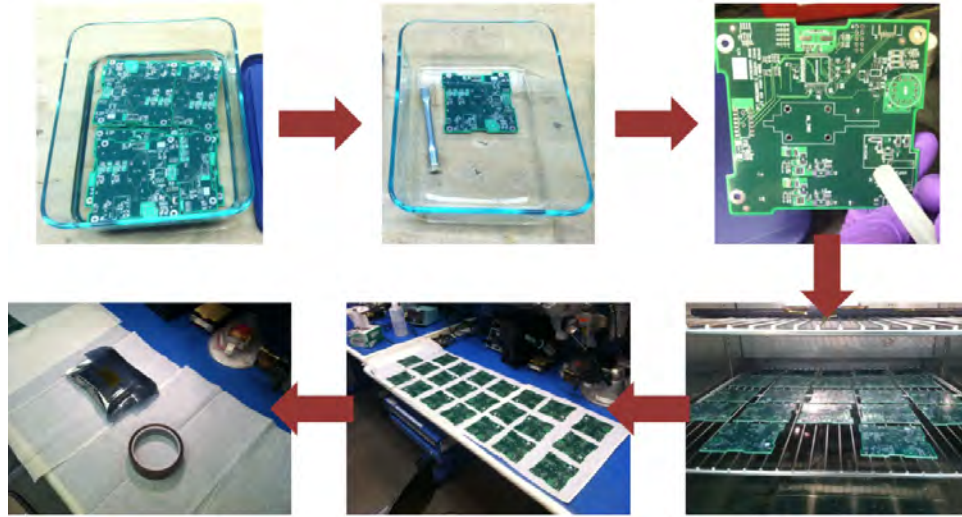


Figure 25: Flow chart showing the initial bare board cleaning

The installation of H1 needed to be done with a certain measure of precision due to the mechanical nature of the EDSN electrical bus. All harnessing in the EDSN spacecraft is done through a vertically mounted circuit board with male header pins installed at the locations of each circuit board in the satellite stack that needed access to the electrical bus. From prior experience with Montana's first satellite it was known that this type of harnessing system is very susceptible to tolerances. All circuit boards in the satellite stack vertically and any deviation in the connectors on a board can result in a large differences between build-up during board-to-satellite integration.

To reduce the amount of error in tolerances between each EPISEM instrument a mechanical jig was manufactured to ensure that the spacecraft bus connectors on all EPISEM boards were in the same exact place and came as close as possible to achieving the  $\pm 0.1$  mm precision required by NASA<sup>2</sup>. As shown in Figure 26, the jig

---

<sup>2</sup>This assembly jig was designed by Andrew Crawford, an undergraduate mechanical engineer at Montana State University

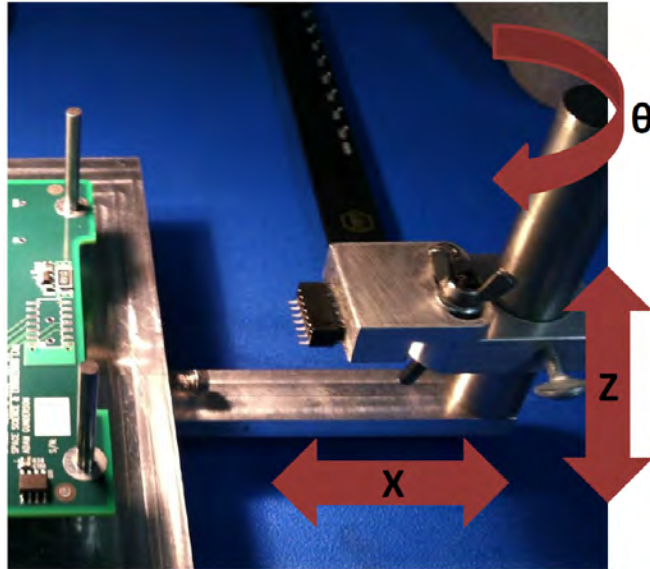


Figure 26: Allowable degrees of freedom of the H1 assembly jig

allows for manipulation in height or  $Z$ , rotation about  $Z$  or  $\theta$ , and the single line distance that the connector would sit from the edge of the board or  $X$ .

Prior to use the jig was calibrated along the  $X$ ,  $Z$ , and  $\theta$  axes by soldering a header on four un-populated boards and minimizing deviation from pin one on the header using caliper measurements. Using the calibrated jig, each flight board could be installed with H1 after it had its stickers removed. Then all boards were given another clean and rinse ethanol bath before being set out to dry on a clean bench. The process from populated board receipt to the installation of H1 is outlined below in Figure 27.

Once the boards were left to dry overnight, they were flashed with software and transitioned to a round of testing before the Geiger tubes were installed, this testing is described in the Instrument Testing Subchapter. After initial tests, each Geiger tube was fitted with a quenching resistor and staked with epoxy into its holder. And once deemed that all boards had passed their first round of testing the Geiger tube assembly was installed onto each board. This was completed by first performing

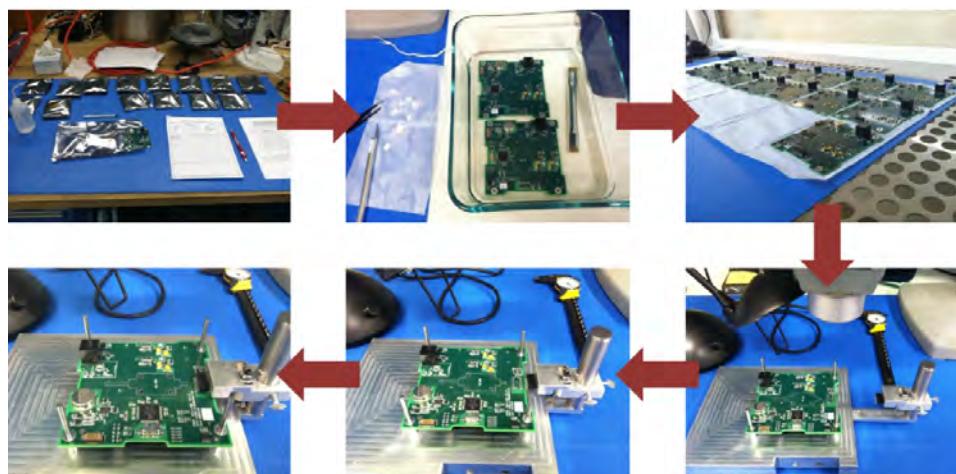


Figure 27: Image showing process of board inspection and H1 installation after the boards were populated with most of components.

a standard double ethanol bath and nitrogen dry cycle; soldering the cathode and quenching resistor to the instrument board; and proceeding to another shallow ethanol bath cycle. The shallow bath was needed in this case due to ethanol dissolving the epoxy restraining the tube inside its holder as well as epoxy connecting the cathode wire to the aluminum shell of the Geiger tube. After this cleaning cycle all boards were baked-out in the thermal chamber at 45 °C for eight hours. The full Geiger tube assembly process is shown in Figure 28.

Once all Geiger tubes were installed on the flight boards another round of acceptance testing was performed. If a boards plateau curve was nominal it would move on to the final phases of assembly. If a tube produced bad results, than it would have to be de-soldered, a Non-conformance report (NCR) written, a new tube installed in its place. Resuming and passing the previous failed test before moving on.

Figure 29 shows the final steps of the assembly process where each board was Staked and Coated using Arathane 5753 and 5750 per NASA Standard 8739.1. The mass of each board being logged between the staking and coating process and after both processes were completed. Finally, each board was flashed with the exact same

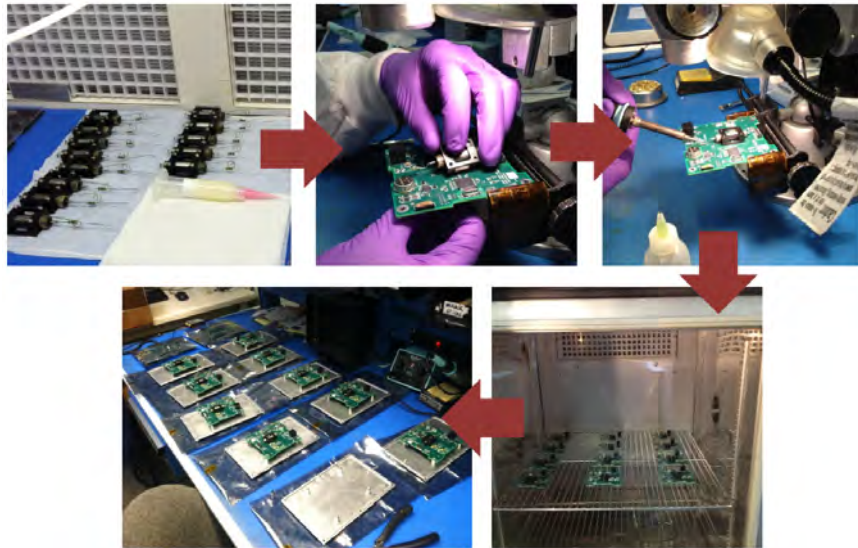


Figure 28: Depiction of the Geiger tube housing assembly and the soldering of the tube assembly onto the circuit board.

flight software and subjected to a final Performance Test which was a smaller subset of the Acceptance test (described in the Instrument Testing subsection). Upon passing this last test each board was packaged into its aluminum shipping box, cleaned, and then double wrapped in ESD safe Kynar. After packaging was completed the boxes were packed, four boards at a time, into a foam lined box and shipped to NASA Ames along with a CD containing each boards documentation packet.

### Instrument Testing

All instrument boards go through three major tests prior to shipping: a Safe-to-Mate which ensures each board turns on properly and has no short circuit current paths; a one time Acceptance Test that characterizes in-rush currents and confirms full operation; and a limited Performance Test, which is a subset Acceptance Test to ensure the board is operating normally. The Performance Test is completed a number of times: after any environmental test or major manufacturing step such as

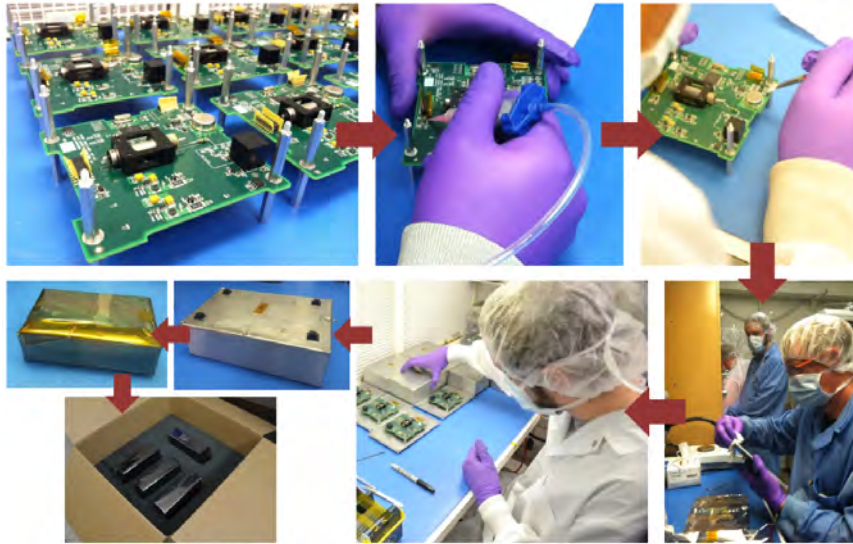


Figure 29: Image displaying the final staking, coating, and packaging process before the instruments were shipped to NASA.

staking and coating, or post integration into the satellite. If any board fails a section of these tests a failure review board is held, depending on the failures severity, and a non-conformance report is drafted to describe what failed and what re-work needs to be done to have the circuit board pass that test step.

### Safe-to-Mate Test

The Safe-to-Mate Test is ran after a board has been populated with all components and installed with H1. None of the boards have a Geiger tube installed during a Safe-to-Mate Test. This test has two major conditions, unpowered and powered, during each condition all external electrical connections are tested. These connections include any connectors, headers, or stand-offs that will interface with another exterior system such as the structure, electrical bus, or ground support equipment. The EPISEM instrument has three of these connections that were put under test: the spacecraft bus connector (H1), the programming connector (H2), and the four structural mounting holes (MT1 - MT4), shown in Figure 30.



Figure 30: Test points measured to ground in the power and unpowered portions of the Safe-to-Mate test.

During the un-powered portion the resistance between each pin and mount hole was measured to ground and compared to its expected value, whether it be a short, open, capacitive, or a static value. Once this test passes for each of the three components the board is then powered, checked to see if its drawing the nominal current and the voltages measured on the three aforementioned components. Once the board completely passes this test it is ready for the Acceptance Test.

### Acceptance Test

The Acceptance Test is a long procedure completed once in each board's lifetime. This test measures very specific characteristics of the board such as switching transients, in-rush currents, ripple voltages, system fault recovery, etc. This is also the first time the instrument is flashed with flight software.

The first procedures involved: software loading, power conversion characterization, and high voltage monitor calibration. The software section of the procedure loaded the board with the testing version of the flight software and then interfaced it with the C&T program over Universal Asynchronous Receiver Transmitter (UART) protocol.

Once interfaced, a proper software load was confirmed and the rest of the test could be completed by commanding the instrument through the C&T program.

Next, the switching waveforms for the 3.3 V and 5.0 V regulators were captured with an oscilloscope. The measured waveform and frequency were checked against the datasheet. While completing this step it was confirmed that the regulators were sourcing approximately 5 mA with  $V_{in} = 8.4$  V, these conditions were also checked against the datasheet.

The images displayed in Figure 31 show the switching waveform (a) and frequency (b) of the 5.0 V regulator. A nominal switching frequency of 50 to 70 kHz under similar operating conditions is shown in (c), taken from the datasheet. Making these measurements on all instruments ensured that the regulators were not operating in a strange or non-optimal state.

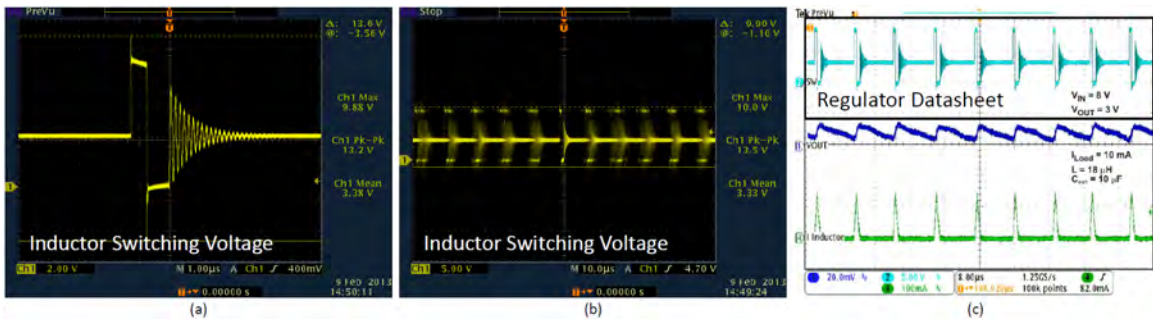


Figure 31: Measured regulator switching waveforms (a and b) waveforms from datasheet (c) [45].

Next, the regulator output ripple voltages were measured, Figure 32 shows examples of the resulting waveforms. Note that output ripple was consistently and below 40 mV for the 3.3 V regulator and below 10 mV for the 5.0 V regulator (Figure 31 top images). When the high voltage power supply was enabled and set to 1000 V, the

output ripple of the 5.0 V regulator decreased slightly (c). This decrease is consistent with the datasheet's output ripple specification shown in Figure 32, (e).

The high voltage supply's output ripple voltage was also measured by probing the output of the resistor divider in the high voltage monitor circuit. Figure 32 (d) shows the typical result from this measurement. The true ripple voltage is 251 times this measured value as the voltage is divided down prior to the test point probed in this section. An output ripple voltage of approximately 15 V is consistent with the datasheet's specification of it nominally being 2% of the output voltage.

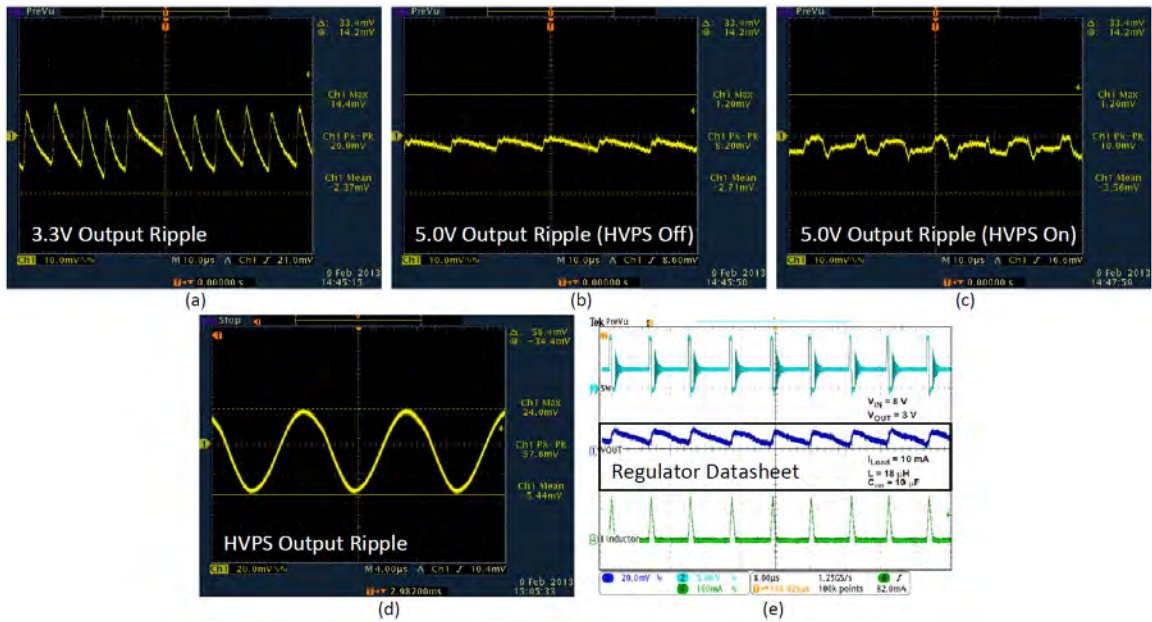


Figure 32: Measured regulator ripple voltages (a,b,c,d) and datasheet ripple voltage (e) [45]

Setting the high voltage power supply to 1000 V in the 5.0 V ripple measurement also tested the high voltage limiter circuit which protects the Geiger tube from damage due to over-voltage. The measurements show that this circuit limited the voltages to approximately 850 V instead of to the designed value: 700 V. This anomaly has

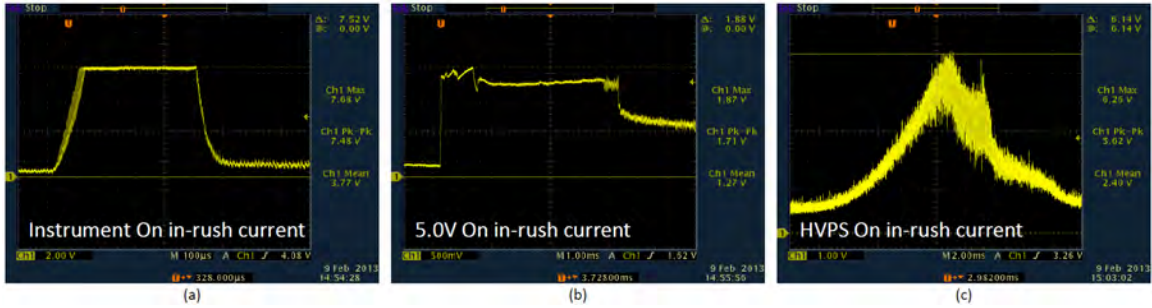


Figure 33: In-rush currents during the instrument power on cycle

likely something to do with the high voltage power supply component, as we noticed that it consistently output almost one-hundred volts more than what it was set it to.

For example, in normal operating mode the high voltage power supply is set to 550 V. This is set by an 8-bit DAC through a non-inverting op-amp with a gain of 1.06 V/V. For a set voltage of 550 V, the calculated output of the 8-bit DAC, before the gain, was set to approximately 2.6 V. Using the high voltage supplies step size of 200 V/V when powered with the DAC the measured output should be around 550 V. However, an offset that is not found at the input to the high voltage supply required the output of the DAC to be scaled back from 2.6 V to 2.19 V (approximately 80 V lower) in order to achieve an HVPS output voltage of 550 V at the HVPS output. For future implementations of this circuit and HVPS this oddity should be analyzed. However, since it did not pose a high risk it was left as designed.

Second, the in-rush current's were characterized, Figure 33 shows the results of this test done under three conditions: 3.3 V regulator turn-on, 5.0 V regulator turn-on, and HVPS turn on to 550 V.

Current in Figure 33 was calculated by applying Equation 8, where 100 is the gain of the current sense amplifier and  $0.910 \Omega$  is the value of the current sense resistor. From Figure 33 noted that none of the in-rush currents are greater than 100 mA and occur over timescales of 20 ms (maximum). This is well below the design specification

of a 150 mA maximum in-rush current over 100 ms.

$$\text{Current} = \frac{\text{Voltage}}{100} * 0.910 \Omega \quad (8)$$

Third, the high voltage monitor circuit was calibrated by taking a truth measurement from the circuit's output using a 1 G $\Omega$  high voltage probe, shown in Figure 34. This truth was then compared to the value read by the PIC24F microcontroller's analog-to-digital converter.



Figure 34: The 1 G $\Omega$  probe and multimeter used to take the truth measurement in the high voltage circuit monitor calibration, meter is currently reading 410V. The oscilloscope in the background is displaying an example of the HVPS ripple voltage, measured earlier.

Because, the high voltage monitor circuit outputs a large voltage scale reading (0 to 1000 V) from small voltage scale measurement (0 to 3.3 V). Any slight changes in component values or amplifier offsets translates into large measurement error (Figure 35). The expected conversion equation for the high voltage monitor circuit, based on the circuit's gains and offset voltages, is shown at the top of Figure 35 (left). In order to bring the measurement error below 5%, a second order equation needed to be applied. Figure 35 (left) shows the error in the high voltage monitor circuit regarding instrument number 21, before applying a second order curve fit.

Figure 35 (right) is the error after the second order curve fit equation (top right) is applied, observe the large decrease in measurement error. Also note that each instrument had its own value for the coefficient tied to the “ $x$ ” portion of the equation.

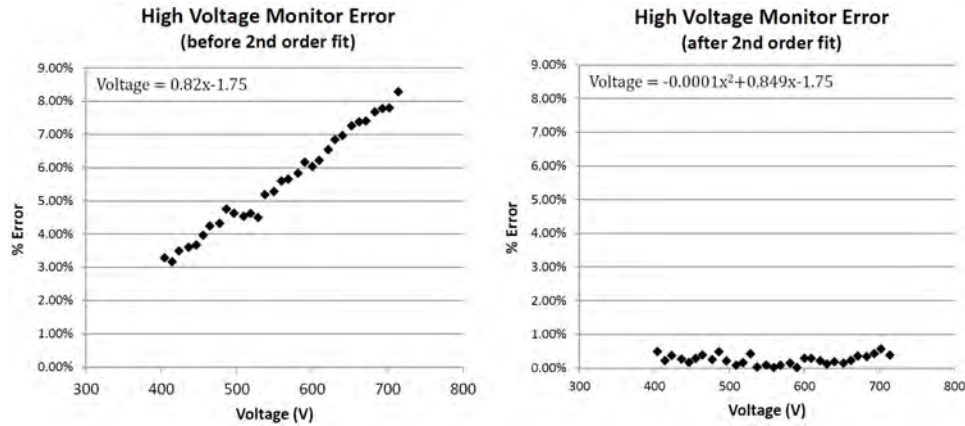


Figure 35: Error in the high voltage monitor circuit for instrument number 21, before (left) and after calibration (right).

The next sections of the Acceptance Test were completed after the Geiger tube was installed. First, the boards power conversion efficiency and power draw was measured by taking current and voltage readings while detecting low and high count rates. This ensured that the regulators were operating within the same parameters across the fifteen instruments. This test was also the first time the Geiger tube was excited with a radiation source and any tubes that produced irregular count rates were replaced before proceeding further.

Following the power regulator test the output pulse of the Amptek was measured while stepping through the different threshold resistor settings. Figure 36 shows how the pulse width is set using an external capacitor ( $C_w$ ). For the EPISEM instrument this capacitor was chosen to be 200 pF. All boards measured output pulses were between 500 ns and 700 ns. This compares well to Figure 36 which shows a nominal pulse

width of 600 ns for the aforementioned value of  $C_w$ . The large range of pulse widths measured were due to changes in threshold setting, making this test also prove that all threshold levels pulse amplifier discriminator were behaving similarly across all instruments.

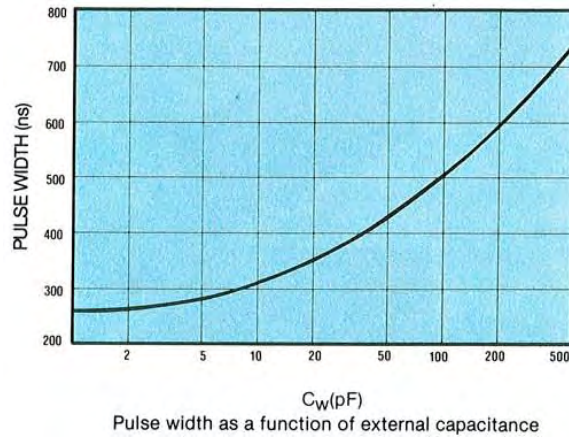


Figure 36: Width of pulse output from the Amptek A101 pulse amplifier discriminator as adjusted by an external capacitor  $C_w$  [46].

Finally, the detector was characterized by analyzing Geiger tube plateau curves. These curves served as an initial calibration point for any future tube testing during the many Performance Tests the boards would undergo. The plateau curves were created by placing a Cobolt-60 radiation source approximately 8 cm away from the center of the Geiger tube, using the radiation source holder GSE. All curves were completed automatically using the Command and Telemetry program and were done at each of the Amptek's threshold levels. Figure 37 are examples of four nominal plateau curves ran at each threshold level. Note that, the slope of the plateau is never zero but is sufficiently low enough to deem the curves indicative of a properly operating Geiger detector. This figure also shows the effect of adjusting the threshold resistance ( $R_t$ ) on the Amptek. Observe that the count rate does not change but the

lower the threshold resistance the higher the turn-on voltage becomes. This is due to the Amptek ignoring pulses from the GM tube until it produces a pulse of sufficient height. On orbit, adjusting these levels may be used to reduce irregular readings from the detector as the instruments amplifier may amplify other signals in the spacecraft.

Once the plateau curves were verified as nominal, the board was ready for the next step in the manufacturing process. If the curves ended up failing this test at any time the Geiger tube would have to be de-installed from the circuit board, removed from its housing and a new tube put in its place. Figure 38 shows two examples of off-nominal plateau curves. The left curve is a passing plateau curve, even though it starts a linear trend upwards after 600 V it has a low enough slope in the plateau region. Figure 38 (right) shows a failed curve. Note that this image, plotted on a log scale, shows a high slope in the plateau region as well as the exponential counts past

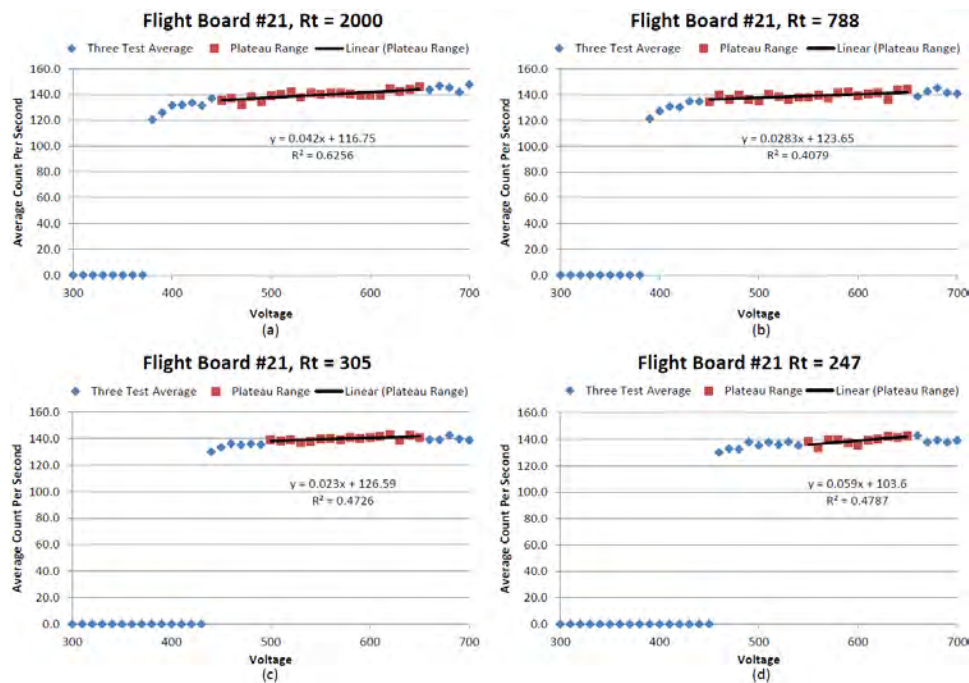


Figure 37: Example of the four plateau curves ran at each threshold setting during the Acceptance Test.

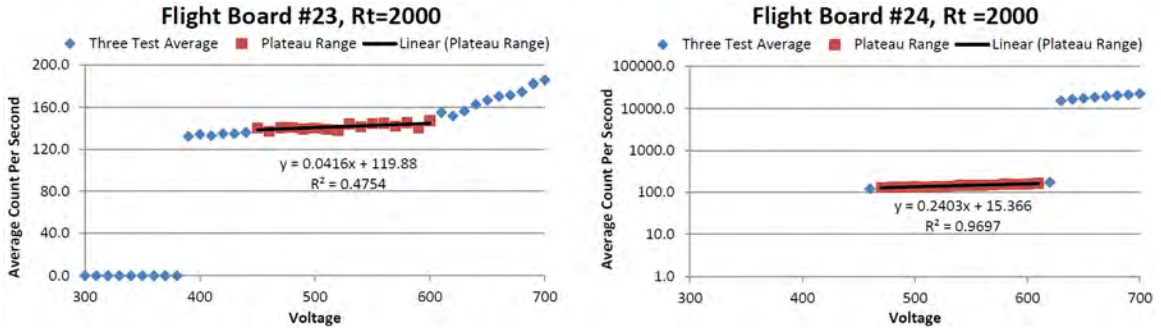


Figure 38: Example of plateau curves, the left curve trends upwards but this curve was still considered a pass due to an optimal slope, right shows an example of a failed plateau curve.

600 V. Out of a stock of twenty-eight tubes, five of them failed on their first plateau test where two others failed after being staked and coated. This may have been due to defects in the tubes manufacturing process or during the assembly process, but further analysis would need to be done. Another possibility links to that around the same time all tubes were being manufactured and packaged, Hurricane Sandy hit the East coast where the manufacture facilities were located.

### Performance Test

The Performance Test is a small subset of the Acceptance Test that ensures the instrument is functioning correctly. This test was completed after any major manufacturing steps such as integration or during an environmental test. This test procedure was written to utilize test scripts written into the C&T program and only included four major measurements: Proper turn-on and current draw, board temperatures, test pulser operation, and a Geiger plateau curve with the default threshold setting. Unlike the Acceptance Test, this procedure was also designed so it could be run without needing physical access to the instrument and test points. This test was ran: After any board re-working, before package and shipment to Ames, after instru-

ment receipt at NASA Ames, pre/post integration into the satellite bus and pre/post environmental testing.

### Test Analysis

A design challenge with this mission was to ensure that all instruments behaved near-identically. If any large deviation in operating parameters was prevalent in any one of the instruments it needed to be discovered on the ground. So on-orbit, if an instrument was producing different count rates than the others, it would be known that it was due to its electronics functioning slightly differently than the others and not due to the radiation environment being measured. To compare test results certain aspects of the test data were taken from the Acceptance and Performance tests and plotted against each other. The primary data points looked at were: in-rush current, power draw, regulator ripple voltages, Geiger plateau slope, and average counts per second across the Geiger plateau.

Figure 39 represents the first three comparisons between the regulator performance on each instrument: in-rush current (a), power draw (b), and ripple voltages (c). The values across all 15 instruments are within the same orders of magnitude, i.e. no single board shows a large deviation in its tested values from the other circuit boards. Note that there is an interesting phenomenon with the high voltage power supply's (HVPS) in-rush current, which seemingly has a lot of deviation. This has to do with how the test was executed and not the power supplies themselves. As stated in the Acceptance Test procedure, to measure the in-rush current when the HVPS is turned on, a test point needs to be probed after setting the power supply to 1000 V (its maximum value). Because the high voltage limiter circuitry doesn't allow the voltage to go that high it will cap the power supply's output voltage at some value. This cap varied greatly between the boards as it

was set with resistors and an operation amplifier. Therefore the large difference in in-rush currents is likely due to the large variations in this upper voltage limit.

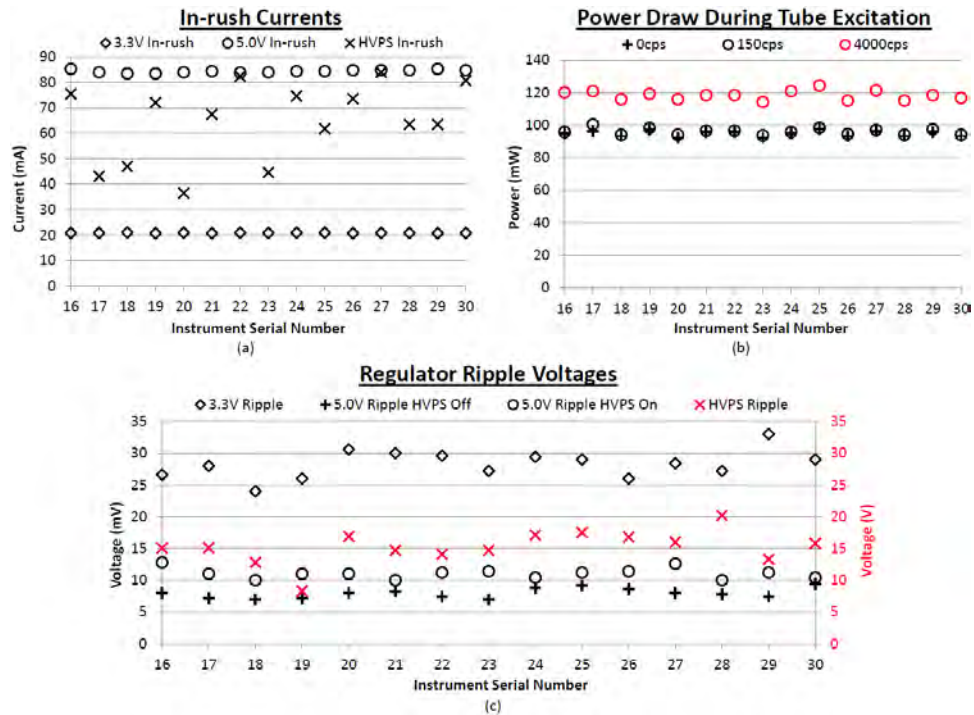


Figure 39: Three plots showing comparison of the results from tests regarding the instruments detector. across all 15 flight units.

Figure 40 displays two specific parameters of the detector electronics measured during the final Performance Test, before shipping the boards to NASA. The two tested values shown are: the slope of the Geiger plateau region (left) and the average counts per second (CPS) across this plateau (right). Note that the left plot shows a rather large deviation from the rest of the slopes on serial number 24. This deviation was caused by the tube not functioning correctly as it appeared to be damaged after the staking and coating process. In this board's case it was deemed that it would stay behind at Montana State since NASA only needs 14 boards

and a total of 15 were assembled. It is not known if this tube broke because it was handled incorrectly during assembly or simply damaged upon its initial manufacture, as happened with some of the other Geiger tubes used on this project.

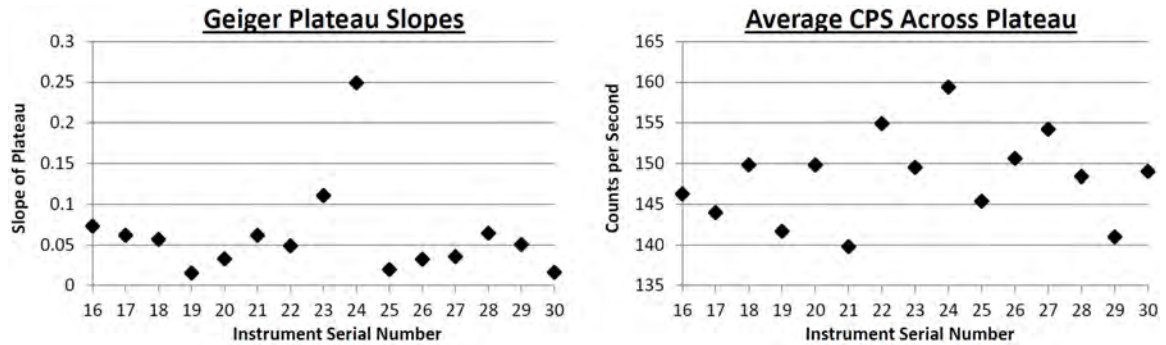


Figure 40: Two plots showing plateau curve comparisons across the 15 assembled and tested instruments.

Finally, deviations from the test values was analyzed to ensure that other more ambiguous problems weren't present with the boards after going through the manufacturing and testing process. This was done by taking the last measured values found in the final Performance Test and calculating its difference from the first values measured in the Acceptance Test. Figure 41 shows an analysis of the chosen values to compare, again note that serial number 24 stands out from the rest as its slope deviates far from the average slopes across all 15 boards (a). This instrument also had a much higher turn-on voltage than the rest of the boards (b). The turn-on voltage representing the level the HVPS' was set to where counts were first present. Additionally, Figure 41 (c) also shows the deviation in the average counts per second across the Geiger plateau region and the boards power draw at a minimum and maximum high voltage levels (d).

Other values not shown in Figure 41 were compared such as: voltage regulator output, counts per second under the test pulser, and A101 output pulse width. These

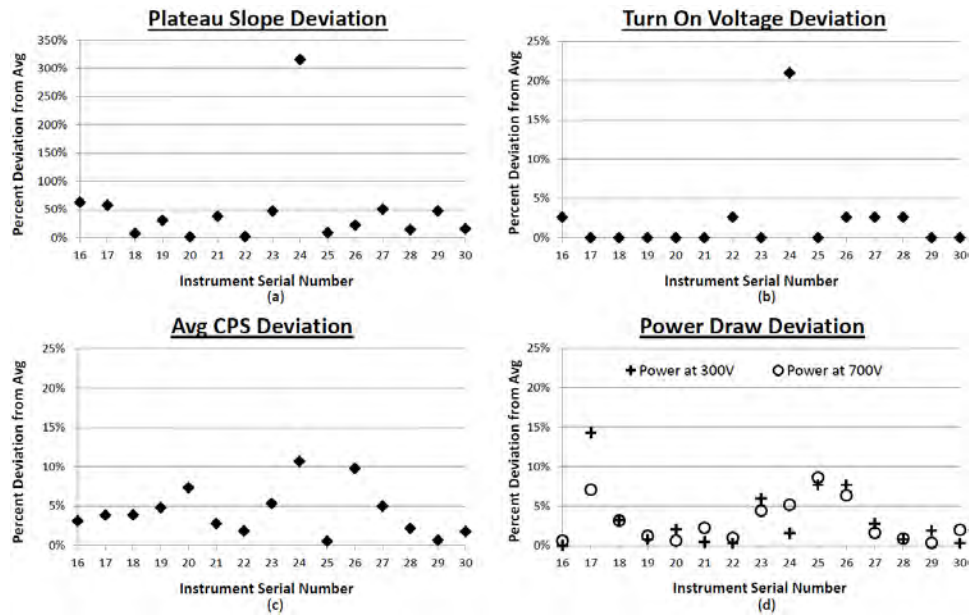


Figure 41: Plots of percent deviation from the average in regards to values tested in the first Acceptance Test and last Performance Test

values are not shown as they had even less deviation than those Figure 41. After comparisons were completed the boards with the eight best plateau slopes and least amount of re-work were chosen as the best EPISEM instruments. These boards would hopefully be placed in the eight flight units that would launch into space. Re-work refers to the fact that some Geiger tubes did not function upon their first time tested with the circuit board. This re-work may have been avoided by testing the tubes stand-alone before installing them into the instrument as it was discovered late in the project that a percentage of the twenty-eight tubes that were ordered, did not function.

### Environmental Testing

The final phase of the test process was environmental testing. For this test phase only one EPISEM board was used due to the length of time it takes to complete these tests and the fact that this type of testing can be hard on the instrument.

The first part of environmental testing involved placing an EPISEM unit in the thermal chamber at ambient pressure and cycling from  $-40\text{ }^{\circ}\text{C}$  to  $40\text{ }^{\circ}\text{C}$ . This ensured that the commercial-off-the-shelf parts would operate within they're specified temperature limits. These temperatures were provided by NASA Ames as the expected temperature extremes the instrument may see on orbit.

Regarding temperatures, the highest risk item on the instrument is the Geiger tube whose temperature limits are:  $-40\text{ }^{\circ}\text{C}$  to  $75\text{ }^{\circ}\text{C}$ . Notice that the lower temperature this board was tested to is below the tubes operating limit. Figure 42 (left) shows the C&T program over the course of the thermal chamber test along with how the board was mounted in the chamber (bottom right). Note that the temperature sensors in this test weren't reporting values below  $-20\text{ }^{\circ}\text{C}$ ; an error in software that was remedied with new code loaded after the test. Each ramp up on the high voltage and other monitors signifies a plateau curve being ran to ensure that the tube has not started to degrade at any point in the test. Figure 42 (top right) shows one of the resulting plateau curves at the lowest temperature bound.

After the thermal chamber test was completed the board was placed in the thermal vacuum chamber (TVAC) to test the instrument over the same temperature ranges but at the pressures seen in the space environment. Figure 43 (left) is a picture of the TVAC chamber used in this test. This specific chamber consists of a base plate, shroud top, and shroud body which are used to heat or cool the chamber with resistor heaters or liquid nitrogen respectively.

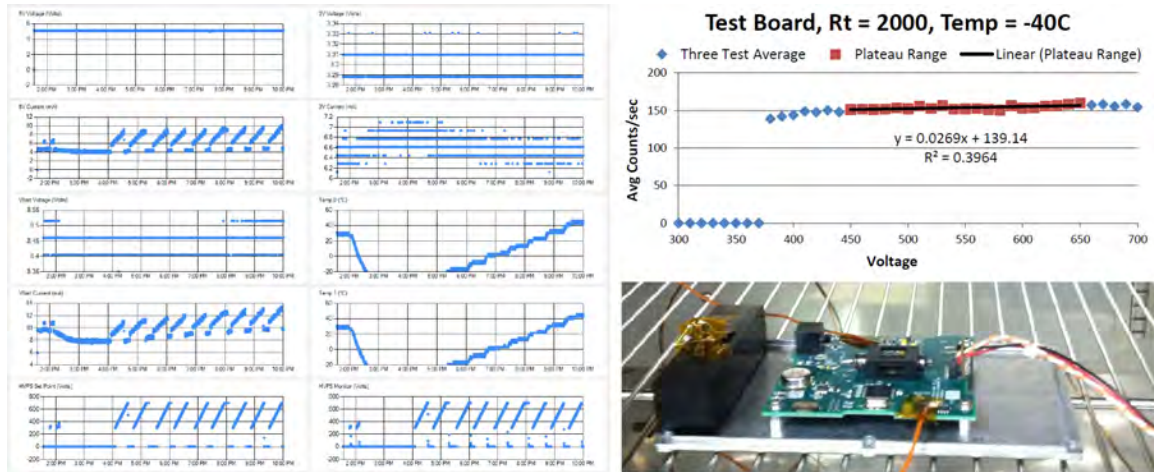


Figure 42: Setup and results from the thermal chamber test.

The instrument was placed in the chamber, mounted to the base plate. Figure 43 (right) shows how the EPISEM board was mounted. After the board was situated two external thermal couples were attached to ensure that it was reaching proper temperature when the instrument was powered off. Once turned on, temperatures were monitored with the instrument's own sensors and the C&T program and checked against external thermal couples.

Once EPISEM was mounted in the chamber the lid was closed and it was pumped down overnight to a pressure of  $10^{-6}$  torr before thermal cycling could begin. Figure 44 outlines the temperature and performance test profile the EPISEM instrument was subjected to. The first cycle to survival temperatures of  $50\text{ }^{\circ}\text{C}$  and  $-50\text{ }^{\circ}\text{C}$  was completed with the instrument turned off. Each of the survival temperatures were held for at least one hour so the board was allowed to “soak” at those temperatures. Once the cold soak was completed, temperatures in the chamber were brought up to the operational limits of  $-40\text{ }^{\circ}\text{C}$  and  $40\text{ }^{\circ}\text{C}$ .

As shown in Figure 44 there were a total of four hot and cold cycles completed in the TVAC test. At each temperature plateau a full performance test was completed

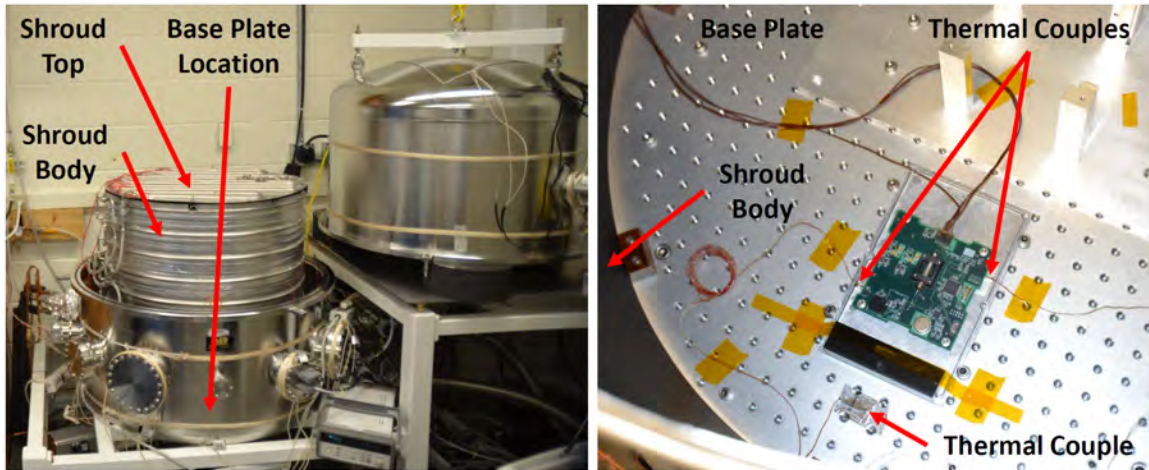


Figure 43: Thermal vacuum chamber test setup showing the heating and cooling elements of the chamber along with where the EPISEM instrument was mounted.

including a Geiger tube plateau curve. Figure 45 shows these cycles with the temperature data recorded by the control thermal couples and temperature sensors aboard EPISEM. On a number of occasions the temperature dropped far below  $-40\text{ }^{\circ}\text{C}$ , this was due to the fact that the thermal vacuum chambers operation in a cold cycle has to be manual, greatly increasing the chance of overshooting the temperature limit.

Figure 46 shows Geiger tube curves ran during the first cold and hot operation plateau's. Note that during the cold cycle, the end of the Geiger plateau is trending exponentially upwards. This may show that the tube could be starting to degrade. However, during the hot test the plateau is shown as much flatter.

After the TVAC was completed and the instrument shelved in ambient pressure for a week it was noticed that the detector ceased to function. From this failure in the TVAC test it was concluded that this board was largely over-tested. Many of the plateau curves were ran below the tubes operating temperature of  $-40\text{ }^{\circ}\text{C}$ . Additionally, at one point in the test, shown in Figure 45, the board temperatures reached  $-60\text{ }^{\circ}\text{C}$ . This was a full 20 degrees below the tubes operating range and most likely cause the seal between the glass and aluminum shell of the tube to crack.

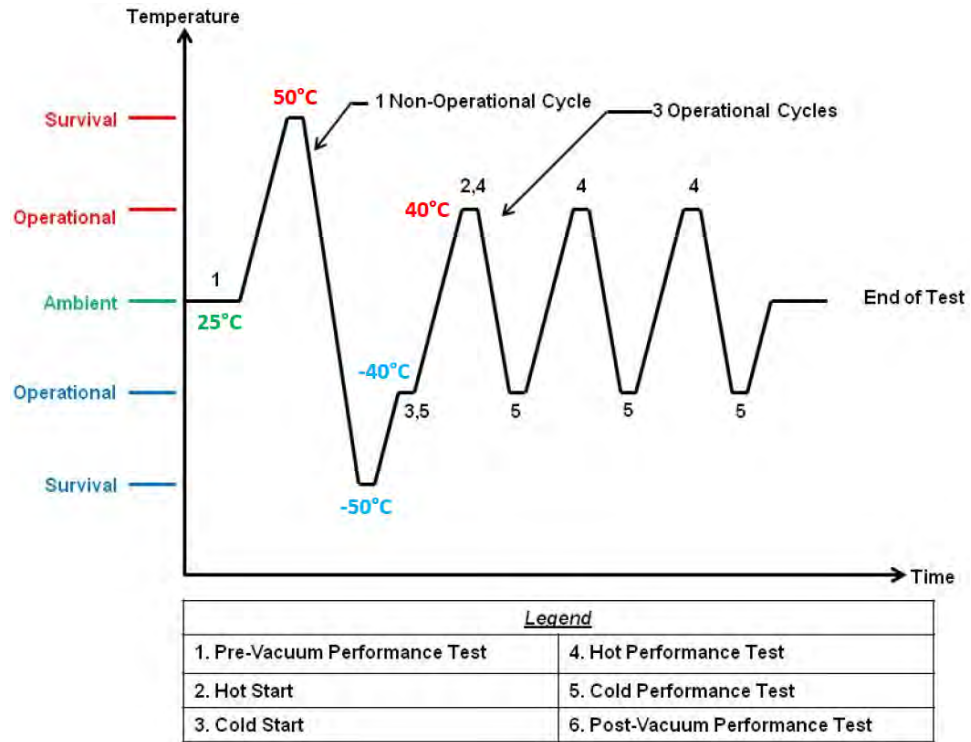


Figure 44: Thermal vacuum chamber temperature profile showing temperature dwell area and the location of Performance Tests

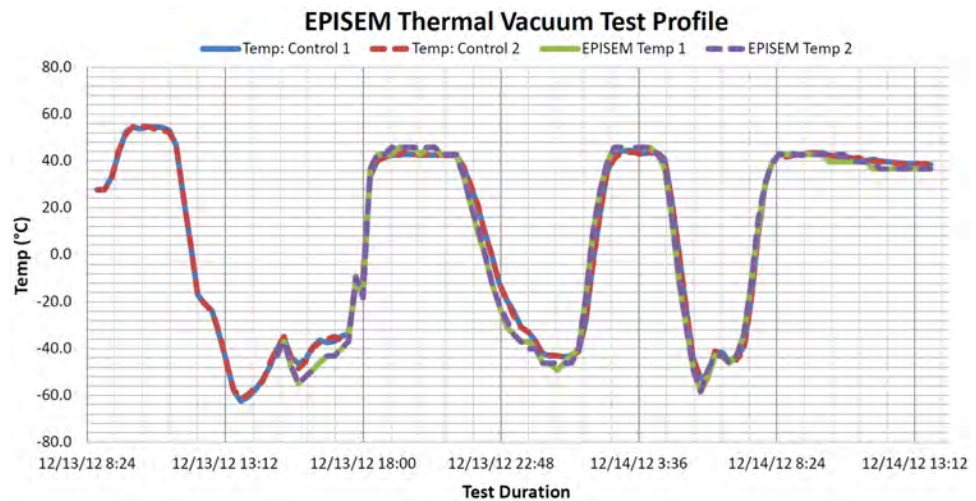


Figure 45: Thermal vacuum chamber temperature data as measured by external thermal couples and temperatures aboard the instrument

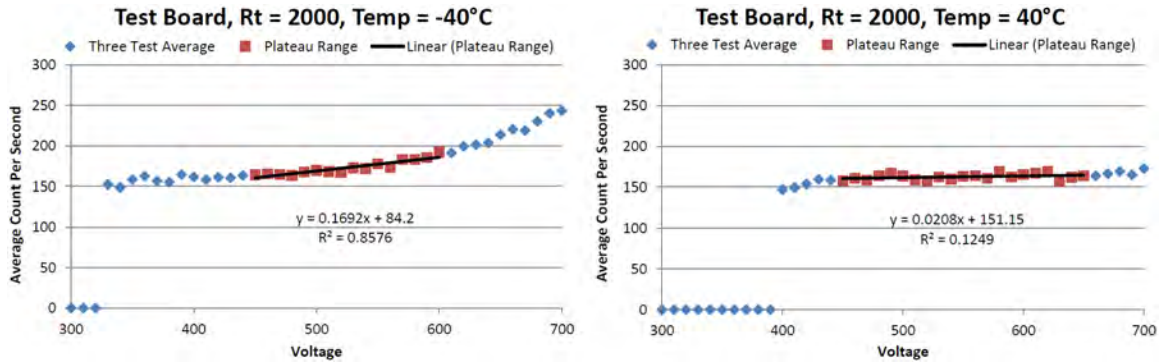


Figure 46: Plateau curves from the first cold (left) and hot (right) temperature plateaus during the thermal vacuum chamber test.

This apparent over testing should have been avoided as the minimum temperatures the tube needed to be tested to were  $-40\text{ }^{\circ}\text{C}$ . This test failure however, did provide information about the tubes specifications as it did continue to operate well below its minimum operating range until brought out of the vacuum chamber.

### High Altitude Balloon Flight

The next test that was performed used the EPISEM test board integrated into a FPGA controlled radiation tolerant computer. This setup was then flown aboard a high altitude balloon with another Geiger tube and a silicon radiation detector. The balloon flight reached approximately 100,000 ft or 28 km and the data from the three detectors is shown in Figure 47 (left) against the expected value taken from a previous balloon flight (right) [23].

As shown, the SparkFun Geiger tube, made by the same company as the SSEL tube (EPISEM), returned much more counts per minute. The approximately doubled count rate is largely due to the increased geometric factor or throughput of the SparkFun tube; which was also almost double that of the EPISEM tube. Both these curves follow the expected result for the radiation at these altitudes (right). This plot also shows the times where the silicon detector possibly measured a heavy ion strike.

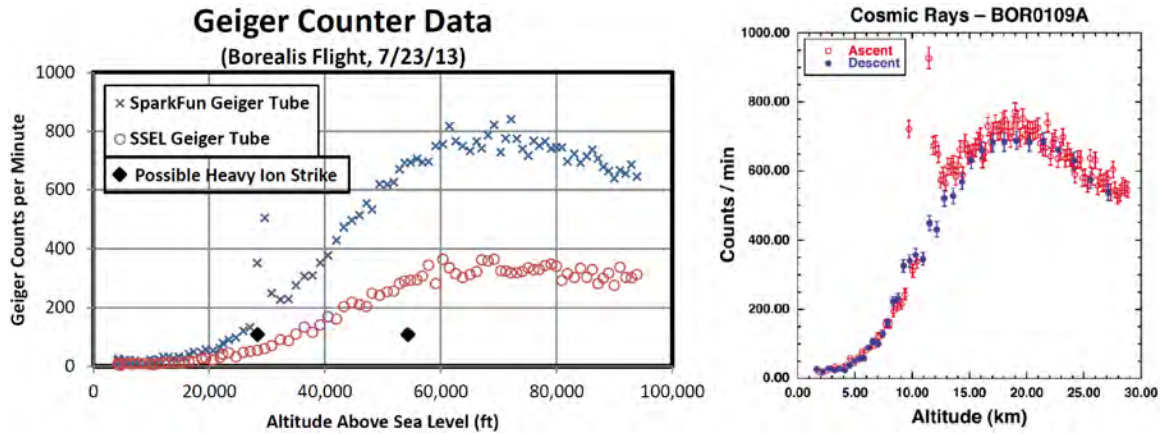


Figure 47: Radiation measured by the instruments aboard the high altitude balloon flight in which EPISEM was tested on (left), image credit: BOREALIS Research Group MSU. Compared against the expected radiation environment from previous balloon flights (right) [23]

This specific silicon detector was fabricated at Montana State University and was set to only detect particles with energies above 40 MeV.

### Satellite Integration and Testing

Finally, after all fourteen instruments were shipped to NASA Ames they could begin the process of being integrated into the full spacecraft bus. Upon receipt at NASA the instruments were subjected to another Performance Test to ensure they survived the shipping process. Once that test passed the instrument could be finally assembled into the spacecraft. Figure 48 (left) shows the EPISEM instrument being plugged into the spacecraft's electrical bus.

Figure 49 shows all the EDSN spacecraft fully integrated, once these spacecraft were built up they were subjected to similar environmental testing in a thermal vacuum chamber and an additional vibration test that simulated launch. The fourteen spacecraft on the left represent all spacecraft including the test units, flight units,

and flight spares. The eight satellites on the right are the chosen flight units that will launch into space.

During the satellite integration and test phase, NASA discovered that the tube on the serial number 22 instrument was not functioning. Because none of the board comparison's show this instrument operating far out of the rest of the fourteen in-

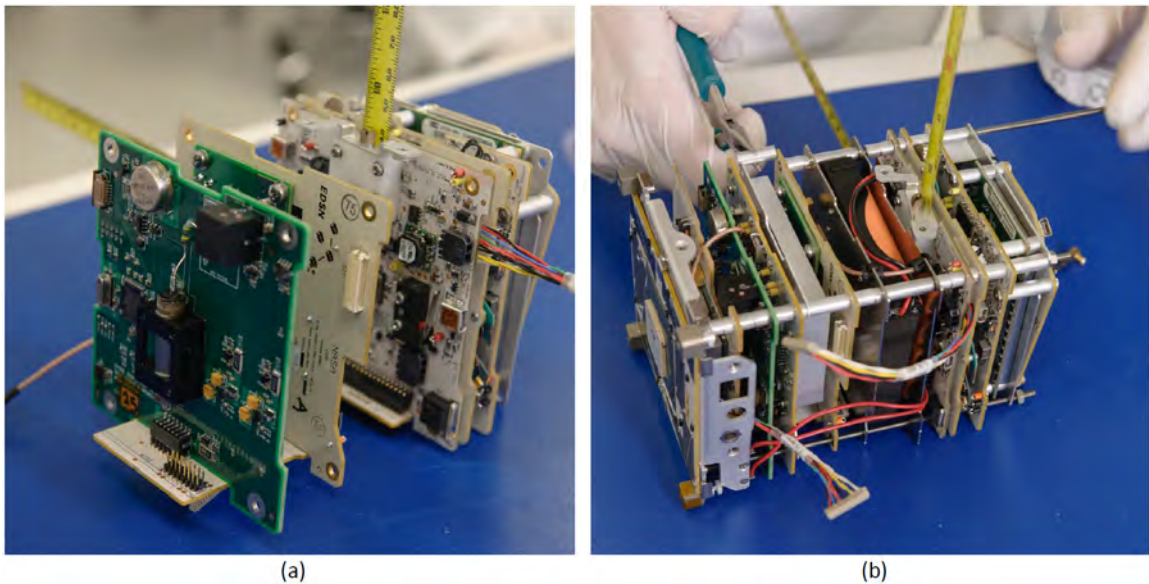


Figure 48: Integration an EPISEM instrument into the EDSN spacecraft electrical bus (left). Continuation of CubeSat stack integration by inserting threaded rods through the structural stand-offs (right) image credit: NASA.

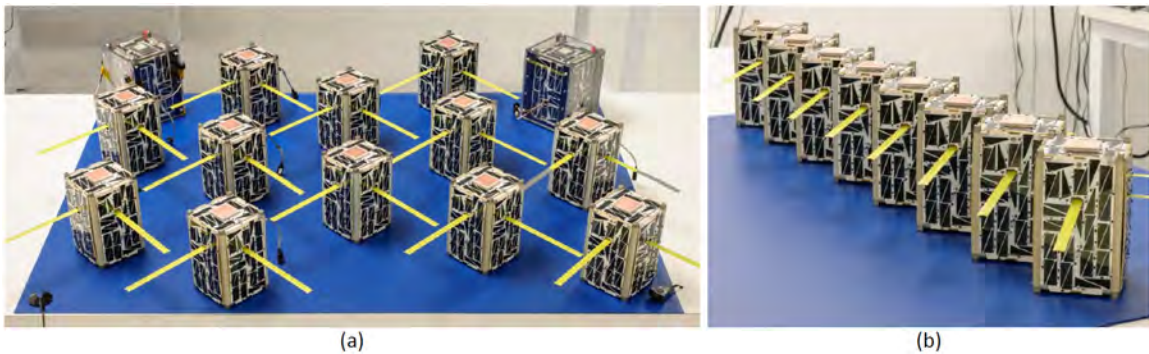


Figure 49: All fourteen of the fully assembled EDSN satellites (left). The eight flight units that will launch into space (right).

struments it is curious to why it failed. However, since the stock of Geiger tubes did seem to have some problems failing after a certain amount of shelf time this failure may be again due to the tubes initial manufacture. Another possibility is that since all of these tubes were continuously tested 50 V above their operating range it could be that this over-testing caused the failure. Further study of this and the other tube failures was not completed for this thesis, an in depth analysis of these specific Geiger tubes may lower some risk in future projects for similar instruments.

## DATA COLLECTION

Once all eight EDSN spacecraft have been deployed to orbit they will begin to function semi-autonomously, collecting data and downlinking that data to the ground via the captain or through a round-robin sixty second beacon. Constantly beaconing instrument and spacecraft state of health as well as last sixty seconds of data collected by the EPISEM instrument. Figure 50 is a depiction of how the satellites will separate from the launch vehicle in space. Note that as deployment from the launch vehicle occurs all eight spacecraft start to congregate into two groups of four. The distance between each group grows much faster than the individual distance between the satellites in their subsequent group. Group 1 is depicted in Green and Group 2 in cyan.

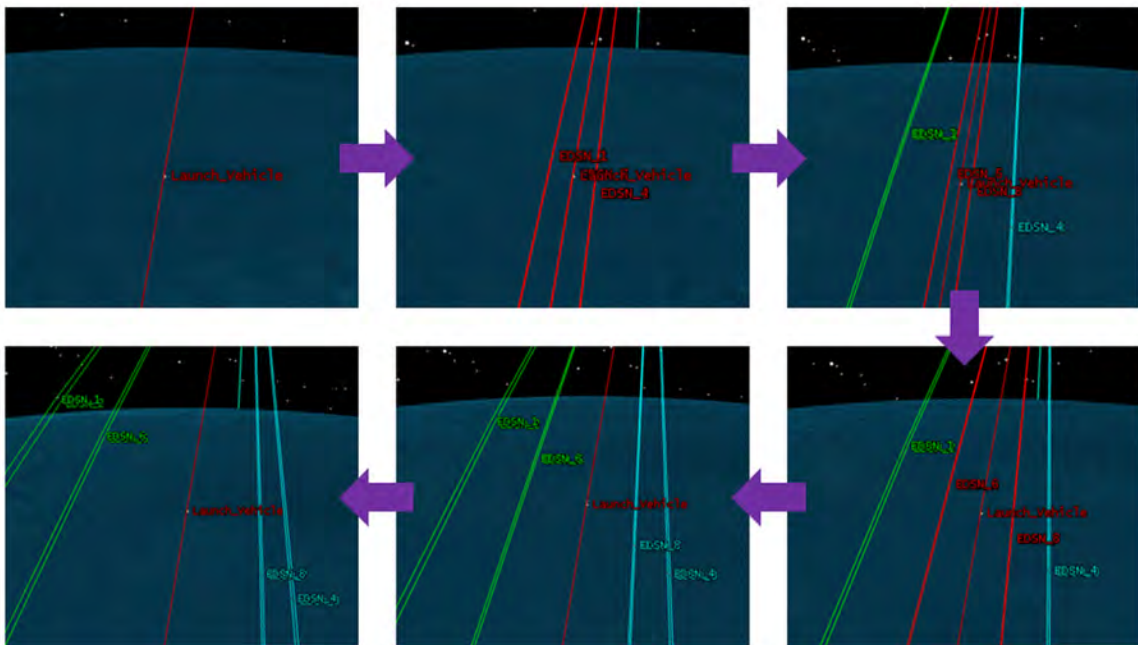


Figure 50: Depiction of the eight EDSN spacecraft as they separate from the launch vehicle into two groups of four spacecraft each, after deployment into space.

As the separation continues, the satellites get further and further apart, although still sticking with their same deployment groups. Figure 51 (left) shows each satellites relative distance from the first spacecraft in Group 1 or EDSN1. The thick lines representing the distances in Group 2 are due to the sinusoidal oscillation prevalent in orbits after these type of CubeSat deployments. The spacecraft in Group 2 simply oscillate much more with respect to EDSN1's location than those in Group 1. Figure 51 (right) displays the two groups separated in orbit with a close up of the distances between the four spacecraft in Group 1 (right corner). These groupings and separations will taking to account when performing analysis of the data collected by the EPISEM instrument.

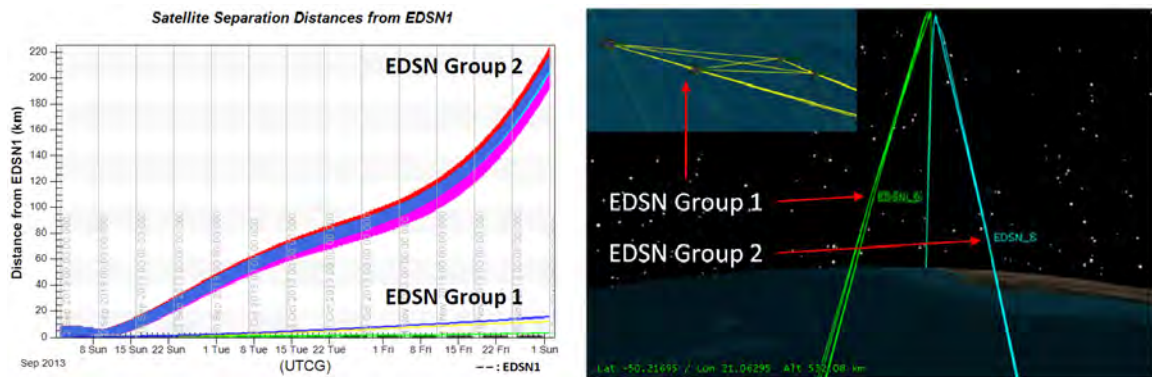


Figure 51: Depiction of how the two groups of EDSN spacecraft separate with respect to the first spacecraft in the swarm (EDSN1) as simulated in Systems ToolKit (STK) from Analytical Graphics Inc

During orbit operations each spacecraft is power and data volume constrained. Therefore, the instrument will only be turned on twice a day for periods of ten minutes each. These data collection periods will not be random but associated with the spacecrafts location in its orbit as set forth in the design objectives. One turn-on location will be between  $30^{\circ}\text{N}$  and  $70^{\circ}\text{N}$  latitude which represents the northern horns of the radiation belts. The other location is within a latitude bound of  $10^{\circ}\text{S}$  to  $50^{\circ}\text{S}$ , this threshold represents the location of the South Atlantic Anomaly. Once

in one of these regions each instrument on all spacecraft in the swarm will be taking data near-simultaneously as the instruments is enabled independently when its parent spacecraft enters the region of interest. The L-shells that these locations correlate to are approximately 0.2 to 2 earth radii for the southern latitudes and 3 to 5 earth radii for the northern latitudes. Figure 52 is a depiction of these locations on the globe in which the instrument will be turned on on a single orbital track. Because of the speed the spacecraft is traveling (7.5 km/s) the ten minute on time will allow it to always collect data in these regions, once per day.



Figure 52: The ten minute periods (shown in yellow) that the instrument will be turned on once a day as simulated in STK

The temporal and spatial resolution with respect to when the instrument is turned on and where it is turned on will be provided by NASA Ames after post-processing data from the EDSN spacecraft avionics. Location accuracy will be within approximately one kilometer and temporal resolution will be one second or better. These resolutions are needed in order to properly analyze the data collected.

Figure 53 (left) is an example of satellite data collected by the SAMPEX mission during one pass through the radiation belts. The dotted blue line represents the satellites trajectory across L-shells, the orange represents an electron microburst phenomenon present in the belts and the black dotted line shows the estimated average flux in the radiation belts. Figure 53 (right) shows a cartoon of radiation belt flux with gross incoherence. From previous studies the expected results would be that all EPISEM satellites would measure average flux along the same dotted red line even with a very small difference in L-shells. What is shown is that each EPISEM instrument is measuring extremely different fluxes indicative of incoherence. What is shown in the right plot is far over exaggerated to what might be measured if there is incoherence along small differences in L-shells.

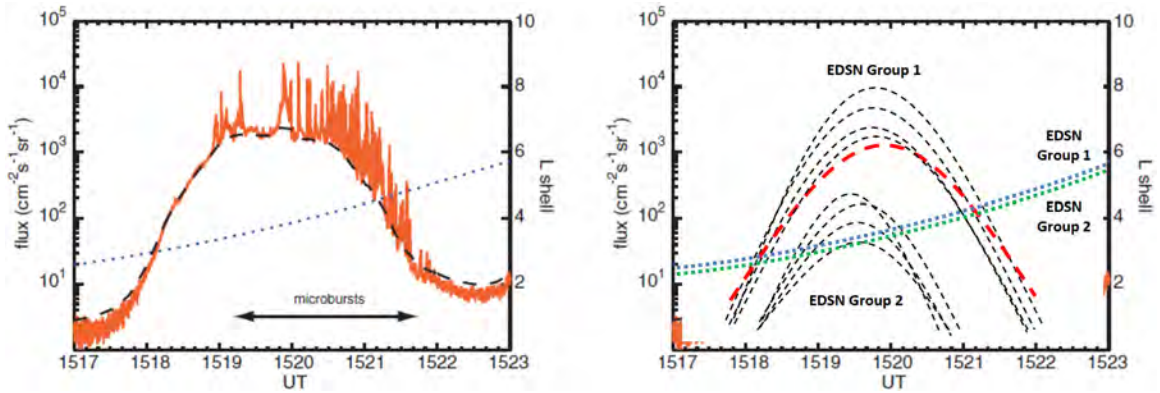


Figure 53: Average flux and electron microbursts in the radiation belts as measured by SAMPEX (left) [24]. Right is a cartoon of gross incoherence in the radiation belts along similar trajectory.

## CONCLUSION

Our growing reliance on space-based technologies have caused the effects of the space weather environment and the Van Allen Radiation Belts on our daily lives to become realized. These highly dynamic regions outside the earth atmosphere are currently not well understood because of a lack of proper measurement. The Energetic Particle Integrating Space Environment Monitor or EPISEM instrument will fill these measurement gaps by taking data across a spatio-temporal array provided by the eight spacecraft EDSN mission. Small spatial and temporal measurement resolutions achieved by this mission will increase the fidelity of current models as well as increasing our fundamental understanding of the space environment.

The EPISEM instrument was designed and built by the Space Science and Engineering Lab at Montana State University. The major design challenges of this project were to ensure all instruments behaved identically as well as being designed to operate in a space environment, use less than 80 mW of power, and generate low data volumes. To meet the environmental requirements one board was subjected to heavy thermal testing at both ambient and low pressures. The rest of the fifteen instruments underwent a very heavy testing cycle in less than six months. The data from these tests was then analyzed to ensure that no electronics in the instruments were behaving far outside a nominal operating range. Results, from these tests showed that only one instrument was behaving far outside the operating ranges of all the other instruments. This board was deemed a spare and the remaining fourteen were marked as flight quality, being shipped off to NASA for integration into the EDSN spacecrafts.

Once all fourteen flight units were sent to NASA Ames they were integrating into fourteen identical spacecraft. A similar testing system where eight spacecraft were

deemed flight units was employed and all satellites are currently awaiting launch in Mid-2014. Once in space the EDSN satellites will turn on the EPISEM instrument twice a day for periods of ten minutes each. Each on period being related to the spatial location of the satellites, in the northern horns of the radiation belts and South Atlantic Anomaly. After collected, these science data will be downlinked to earth through the EDSN spoke-type network topology so it may be cataloged, stored, and analyzed.

### Lessons Learned

The main driver of this project in terms of schedule was the speed in which it needed to be completed. Because of this some tests were left out that should have been done. One of these tests was that all Geiger tubes should have been tested to ensure operation before they were installed onto each of the fifteen instruments. Since these tests were not completed many of the tubes were found to be not working after installation and it was unknown to whether our installation process was at fault or the stock of tubes was poor.

Additionally, two tubes that were functioning normally after installation also failed after a certain amount of time without being subjected to any different processes or testing. This leads to a need to purchase the detectors far before integration and subjected to tests every month or so to ensure that the tubes will have a longer life. Though all these problems with the Geiger tubes may have been due to an issue at the manufacturer as they supplied all the detectors around the same time as a hurricane flooded their shop.

A major lesson learned with this project that cause all boards to be re-made was due to a mechanical tolerance error. This mistake happened because of a sign error

in the circuit board design program, it could have been caught if a solid model was output from this program and imported into SolidWorks. Instead, a drawing was re-created by hand in SolidWorks and given to NASA without the true mechanical dimensions of the manufactured board as it did not include the sign error. To avoid this type of mix up in the future it is recommended that all future circuit board designs include an output to a 3D mechanical design program such as SolidWorks so the true dimensions are known.

Lastly, a lesson was learned on this project about over-testing. As only one EPISEM board went through environmental testing, it was subjected to much harsher environments than the rest of the instruments. Some of these environments ended up being far outside the operating range of the detector and likely damaged the detector during testing. This somewhat nullified the thermal vacuum chamber test as its main purpose was to see if the instrument could survive at certain temperatures. Since the temperatures in the test were overshoot and reached almost twenty degrees below the detectors operating range, this ended up damaging the tube.

### Future Work

This research solely focused on the development and characterizations of the EPISEM instrument that will be launched into space late-2014. There is work that should be completed before and after data is collected by the instrument. Too properly characterize the detector a Geant4 model needs to be completed using the EDSN structure, this will get a proper prediction of the energy above which the Geiger tube will integrate when collecting data.

Additionally, research into possible ways of predicting responses of the EPISEM detector at small spatial and temporal scales needs to be completed. During the

research for this paper it was discovered that research into this subject is difficult without the proper physics background. A better understanding of the particle physics behind the phenomenon of the radiation belts would help in the possible development of radiation belt models on small spatio-temporal scales.

Finally, work still needs to be completed in setting up how the data will be stored and processed at Montana State University. The data will be initially stored by NASA Ames after being time and location tagged. However, after this there is still post-processing that needs to be done to scale the counts per second collected by instruments by the tubes geometric factor. A great area of study would also be to produce a unique way of analyzing the data across all instruments in some simultaneous fashion. These will help process the data as each data product from each instrument will be separating in space and sometimes in time as each satellite will enter and exit the regions of data collection at slightly different times.

## REFERENCES

- [1] J.W. Allison “Gamma-Radiation Absorption Coefficients of Air in the Energy Range of 0.01 to 100 MeV”. *Journal of Applied Physics*, vol. 29, no. 8, pp. 1175-1178, August 1958.
- [2] D.N. Baker, J.B. Blake, R.W. Klebesadel et al. “Highly Relativistic Electrons in the Earth’s Outer Magnetosphere 1. Lifetimes and Temporal History 1979-1984”. *Journal of Geophysical Research*, vol. 91, no. A4, pp. 4265-4276, April 1986.
- [3] D.N. Baker, J.B. Blake, L.B. Callis et al. “Relativistic Electrons Near Geostationary Orbit: Evidence for Internal Magnetospheric Acceleration”. *Geophysical Research Letters*, vol. 16, no. 6, pp. 559-562, July 1989.
- [4] D.N. Baker, G.M. Mason, O. Figueroa, et al. “An Overview of the Solar, Anomalous, and Magnetospheric Particle Explorer (SAMPEX) Mission”. *IEEE Transactions on Geoscience and Remote Sensing*, vol. 31, no. 3, pp. 531-541, May 1993.
- [5] D.N. Baker, J.B. Blake, L.B. Callis, et al. “Relativistic electron acceleration and decay time scales in the inner and outer radiation belts: SAMPEX”. *Geophysical Research Letters*, vol. 21, no. 6, pp. 406-412, March 1994.
- [6] J.L. Barth, C.S. Dyer, E.G. Stassinopoulos “Space, Atmospheric, and Terrestrial Radiation Environments”. *IEEE Transactions on Nuclear Science*, vol. 50, no. 3, pp. 466-481, June 2003.
- [7] W. Baumjohann, R.A. Treumann *Basic Space Plasma Physics*. “Imperial College Press”, London, 1996.
- [8] G.A. Bazilevkaya, I.G. Usoskin, E.O. Fluckiger, et al. “Cosmic Ray Induced Ion Production in the Atmosphere”. *Space Science Review*, vol. 137, pp. 149-173, March 2008.
- [9] M.J. Berger, J.S. Coursey, J. Chang “ESTAR, PSTAR, and ASTAR: Computer Programs for Calculating Stopping-Power and Range Tables for Electrons, Protons, and Helium Ions”. *National Institute of Standards and Technology* Greenburg MD, ver. 1.2.3, Internet: <http://physics.nist.gov/Star> [August 2013].
- [10] P. Buehler “Radiation Belts”. *Paul Scherrer Institute*, Switzerland, 1998.
- [11] J. Cockrell, D.M. Klumpar “EDSN: A Large Swarm of Advanced Yet Very Affordable, COTS-based NanoSats that Enable Multipoint Physics and Open Source Apps”. *AIAA/USU Conference on Small Satellites*, SSC12-I-5, August 2012.

- [12] E.J. Daly, J. Lemaire, D. Heynderickx, et al. “Problems with Models of the Radiation Belts”. *IEEE Transactions on Nuclear Science*, vol. 43, no. 2, April 1996.
- [13] R.H.W. Friedel, G.D. Reeves, T. Obara “Relativistic electron dynamics in the inner magnetosphere – a review”. *Journal of Atmospheric and Solar-Terrestrial Physics*, vol. 64, no. 2002, pp. 265-282, May 2001.
- [14] G.P. Ginet, T.P. O’Brien. “AE-9/AP-9 Trapped Radiation and Plasma Models, Requirements Specification” *Air Force Research Laboratory*, March 2009.
- [15] G.P. Ginet, T.P. O’Brien, S.L. Huston, et al. “AE9, AP9 and SPM: New Models for Specifying the Trapped Energetic Particle and Space Plasma Environment” *Space Sci Rev*, vol. 179, pp. 579-615, US Government, March 2013.
- [16] W.L. Imhof, H.D. Voss, J. Mobilia, et al “Relativistic Electron Enhancements: Simultaneous Measurements from Synchronous Low Altitude Satellites.”. *Geophysical Research Letters*, vol. 18, no. 3, pp. 397-400, March 1991.
- [17] S.G. Kanekal, D.N. Baker, B. Klecker, et al. “Magnetospheric response to magnetic cloud (coronal mass ejection) events: Relativistic electron observations from SAMPEX and POLAR”. *Journal of Geophysical Research*, vol. 104, no. A11, pp. 24885-24894, November 1999.
- [18] S.G. Kanekal, D.N. Baker, J.B. Blake “Multisatellite measurements of relativistic electrons: Global coherence”. *Journal of Geophysical Research*, vol. 106, no. A12, pp. 29721-29732, December 2001.
- [19] S.G. Kanekal, D.N. Baker, R.L. McPherron “On the seasonal dependence of relativistic electron fluxes”. *Annales Geophysicae*, vol. 28 pp. 1101-1106, May 2010.
- [20] M.G. Kivelson, C.T. Russell *Introduction to Space Physics*. Cambridge University Press, Cambridge MA, 1995.
- [21] G.F. Knoll “Radiation Detection and Measurement”. John Wiley and Sons, 3rd edition, 1999.
- [22] K.R. Lang *The Cambridge Encyclopedia of the Sun*. Cambridge University Press, Cambridge MA, 2001.
- [23] S.L. Larson, J.C. Armstrong, W.A. Hiscock “The first frontier: High altitude ballooning as a platform for student research experiences in science and engineering”. *American Journal of Physics Teachers*, vol. 77, no. 6, pp. 489-497, June 2009.

- [24] K.R. Lorentzen, M.D. Looper, J.B. Blake “Relativistic electron microbursts during the GEM storms”. *Geophysical Research Letters*, vol. 28, no. 13, pp. 2573-2576, July 2001.
- [25] C.A. Lundquist, R.J. Naumann, A.H. Weber “Directional Flux Densities and Mirror-Point Distributions of Trapped Particles from Satellite 1958 $\epsilon$ ”. *Journal of Geophysical Research*, vol. 67, no. 11, pp. 4125-4133, October 1962.
- [26] I.R. Mann, E.A. Lee, S.G. Claudepierre, et al. “Discovery of the action of a geophysical synchrotron in the Earth’s Van Allen radiation belts”. *Nature Communications*, vol. 4:2795, no. 3795, November 2013.
- [27] C.E. McIlwain “Coordinates for Mapping the Distribution of Magnetically Trapped Particles”. *Journal of Geophysical Research*, vol. 66, no. 11, November 1961.
- [28] T.G. Northrop, E. Teller “Stability of the Adiabatic Motion of Charged Particles in the Earth’s Field”. *Physical Review*, vol. 117, no. 1, pp. 215-225, January 1960.
- [29] R.C. Olsen *Introduction to the Space Environment*. University of California, 2005.
- [30] J.M. Palmer “Radiometry and photometry FAQ”. *Optical Sciences Center, University of Arizona, Tucson AZ*, October 2003.
- [31] J.A. Shaw Lecture in Electro-Optical Systems. Topic: “Basics of Radiometry and Photometry”, Montana State University, 2012.
- [32] W.N. Spjeldvik, P.L. Rothwell “The Radiation Belts” in *Handbook on geophysics and spacephysics*. Final Report, A.S. Jurse (ed.). Air Force Geophysics Laboratory, US Government 1985.
- [33] D.P. Stern, N.F. Ness “Planetary Magnetospheres” In: Annual review of astronomy and astrophysics. *Annual Reviews Inc*, vol. 20, pp. 139-161, Palo Alto CA, 1982.
- [34] J.A. Van Allen, C.E. McIlwain, G.H. Ludwig “Radiation Observations with Satellite 1958 $\epsilon$ ”. *Journal of Geophysical Research*, vol. 64, no. 3, pp. 271-286, March 1959.
- [35] J.A. Van Allen, L.A. Frank “Radiation Around the Earth to a Radial Distance of 107,400 km”. *Nature*, vol. 183, no. 4659, pp. 430-434, March 1959.
- [36] D. Vassiliadis, A.J. Klimas, R.S. Weigel, et al. “Structure of the Earth’s outer radiation belt inferred from long-term electron flux dynamics.”. *Geophysical Research Letters*, vol. 30, no. 19, pp. 4.1-4.5, October 2003.

- [37] V. Vouk “Projected Area of Convex Bodies”. *Nature*, vol. 162, no. 4113, pp. 330-331, August 1948.
- [38] *Dynamics of the Earth’s Radiation Belts and Inner Magnetosphere* D. Summers, I.R. Mann, D.N. Baker, and M. Schulz, editors. Geophysical Monograph. American Geophysical Union, Washington DC, 2012.
- [39] *Effects of Space Weather on Technology Infrastructure*, I.A. Daglis (ed.). Springer Science and Business Media Inc, 2005.
- [40] “Guide to Modeling Earth’s Trapped Radiation Environment”. *American Institute of Astronautics and Aeronautics*, Reston VA, 1999.
- [41] *IADC Space Debris Mitigation Guidelines*. Inter-Agency Space Debris Coordination Committee, IADC-02-01, rev. 1, September 2007.
- [42] *The Sun to the Earth – and Beyond: A Decadal Research Strategy in Solar and Space Physics*. National Academies of Sciences, Washington DC, 2003.
- [43] *Solar and Space Physics: A Science for a Technological Society*. National Academies of Sciences, Washington DC, 2013.
- [44] “CubeSat Design Specification” CubeSat Program. *California Polytechnic State University*, rev. 12, February 2014.
- [45] “15V, 75mA High Efficient Buck Converter”. *Texas Instrument Inc.*, Datasheet, July 2010.
- [46] “Charge Sensitive Preamplifier-Discriminator A101”. *Amptek Inc.*, Datasheet.

APPENDIX A

INSTRUMENT SPECIFICATIONS

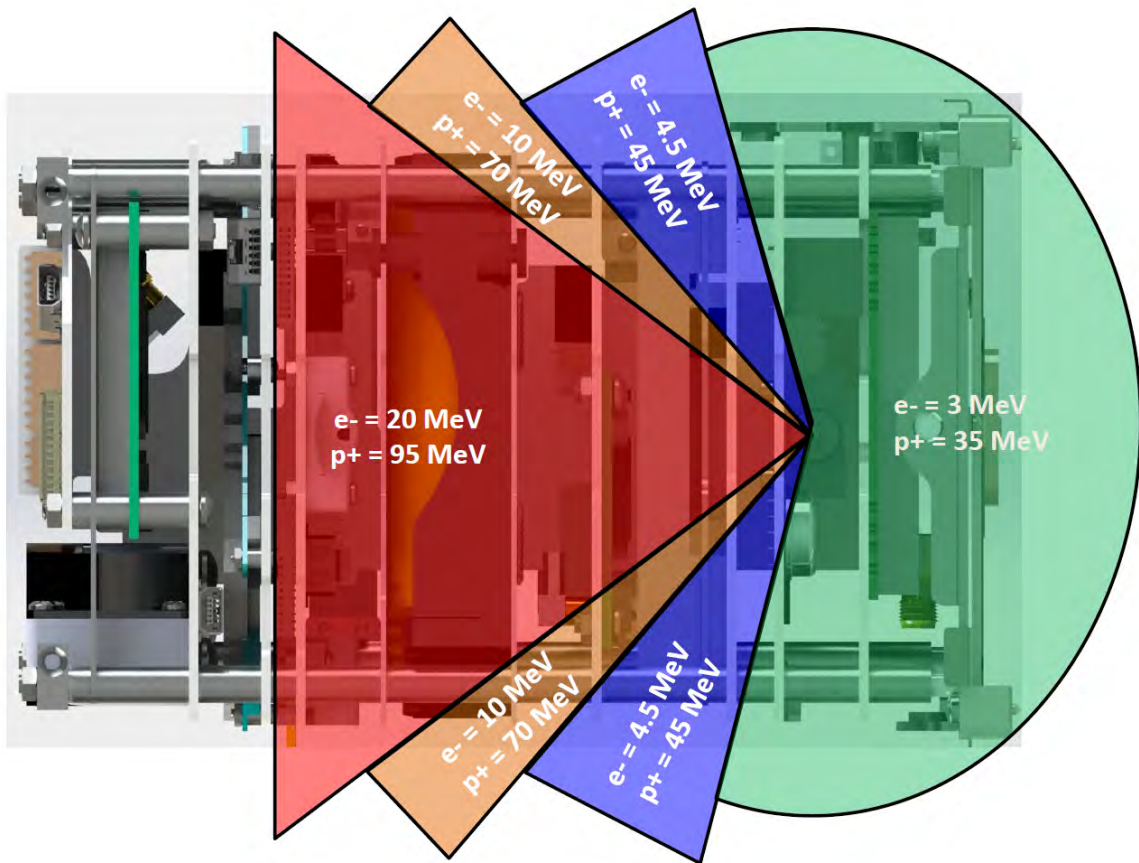


Figure 54: Depiction of the major angles of entry and their energy threshold for the non-uniform EDSN structure.

Table 4: Operating Specifications for the EPISEM Instrument based on test data from the 15 assembled units.

<b>Parameter</b>	<b>Min</b>	<b>Max</b>	<b>Typ.</b>	<b>Unit</b>
Instrument Operating Voltage	5.5	15	8.4	V
Instrument Operating Power	90	120	110	mW
Instrument Operating Temperature	-40	40	25	°C
Detector Operating Voltage	450	650	550	V
Electron Energy Threshold	3	5		MeV
Proton Energy Threshold	35	45		MeV
Geiger Tube Dead-time	40	50	45	μs
Geiger Tube Plateau Slope	0.01	0.1	0.05	
CPS before dead-time effects		10000		counts/sec
CPS deviation across all detectors			10	%